

Open Cluster Study Using *Gaia* I: Membership and Cluster Properties

ANINDYA GANGULY ¹, PRASANTA K. NAYAK ^{1,2} AND SOURAV CHATTERJEE ¹¹ *Tata Institute of Fundamental Research, Department of Astronomy and Astrophysics, Homi Bhabha Road, Navy Nagar, Colaba, Mumbai, 400005, India*² *Instituto de Astrofísica, Pontificia Universidad Católica de Chile, Av. Vicuña MacKenna 4860, 7820436, Santiago, Chile*

ABSTRACT

Star clusters are interesting laboratories to study star formation, single and binary stellar evolution, and stellar dynamics. We have used the exquisite data from *Gaia*'s data release 3 (DR3) to study 21 relatively rich and nearby open clusters with member numbers (N_{cl}) > 500. We have developed a non-parametric method to identify cluster members. Our method works well for clusters located in both sparse and crowded environments, hence, can be applied to a wide variety of star clusters. Since the member classification scheme does not make any assumptions on the expected distributions of potential cluster members, our method can identify members associated with clusters that are oddly shaped or have complex internal spatial or kinematic structures. In addition, since the membership determination does not depend on the proximity to any well-defined sequences on the color-magnitude diagram, this method easily identifies straggler members. Furthermore, for each of these clusters, we estimate essential cluster properties including age, metallicity, distance, and reddening using detailed Markov-Chain Monte Carlo parameter estimation. We report the full posteriors for these important cluster properties for all clusters in our study.

Keywords: open star clusters

1. INTRODUCTION

It is believed that stars are born in groups of a variety of sizes, some of which disperse and populate the field, while the others remain gravitationally bound to form star clusters we observe today (Lada & Lada 1991; Brasser et al. 2006; Kruijssen et al. 2011; Pfalzner et al. 2012; Parmentier & Pfalzner 2013). Among the most manifest objects in the sky, star clusters are interesting for many branches of astrophysics because they are the sites of the highest density of mostly coeval aggregate of stars with similar metallicity ([Fe/H]) within a given angular scale. Star clusters have often been used for constraining single and binary stellar evolution (Leiner & Geller 2021). The age (t_{age}), [Fe/H], and the main-sequence (MS) turn-off of a star cluster can be constrained from its colour-magnitude diagram (CMD) with a much greater accuracy compared to individual stellar objects. Because of the clearly defined CMDs, a plethora of exotic stellar sources such as blue-stragglers (BSs, e.g., Sandage 1953; Johnson & Sandage 1955; Geller & Mathieu 2011; Geller et al. 2012; Gonnell et al. 2014; Brogaard et al. 2018; Sindhu et al. 2019;

Sahu et al. 2019; Leigh et al. 2019), sub-subgiant stars (SSGs, e.g., Geller et al. 2017; Leiner et al. 2017; Geller et al. 2017), and MS-white dwarf (WD) binaries (Pal & Jadhav 2024; Grondin et al. 2024) are easier to identify in star clusters. In addition, dense star clusters are efficient factories of exotic stellar sources formed via various dynamical and binary stellar evolution processes active in them (Knigge et al. 2009; Bhattacharya et al. 2019; Nine et al. 2020; Rain et al. 2020; Vaidya et al. 2020).

The relatively less dense, young, and metal-rich star clusters in the Milky Way (MW) disk are usually called open clusters (OCs). The OCs in the MW exhibit a wide range in t_{age} , spanning a few Myrs to several Gyrs (e.g., Cantat-Gaudin 2022). OCs have been studied for a very long time, some of the first studies date back to the time of naked-eye observations. In the age of modern astronomy, many past surveys have already identified and studied OCs in the MW (e.g., Dreyer 1888). However, the large and precise astrometric and photometric survey data provided recently by *Gaia* (Gaia Collaboration et al. 2022) have significantly improved our ability to identify OCs and ascertain membership of objects within them.

Since OCs are within the MW disk and have much lower stellar densities compared to their more massive and older counterpart, the globular clusters (GCs), it is usually very hard to determine stellar membership for

OCs, especially out to a large-enough distance from the OC’s fiducial center. In the pre-*Gaia* era, the state-of-the-art was detailed focused observations of specific rich OCs which allowed extraction of stellar populations in the target cluster with great details (e.g., von Hippel & Sarajedini 1998; Sarajedini et al. 1999; Tofflemire et al. 2014; Thompson et al. 2014). With *Gaia*’s precise astrometric and photometric data the priorities have shifted towards the identification of vast numbers of OCs and characterisation of membership to a limited distance from the fiducial density centre using primarily machine-learning (ML) algorithms (e.g., Cantat-Gaudin et al. 2018a,b, 2019; Castro-Ginard et al. 2021; Kounkel et al. 2020; Hunt & Reffert 2021). In particular, thousands of OCs were identified using *Gaia*’s DR2 and several previously identified OC candidates were re-futed as asterisms (Cantat-Gaudin et al. 2018a,b, 2019, hereafter collectively CG-DR2). Some other studies employed various parameterised statistical techniques such as gaussian mixtures to identify cluster members using proper motion ($\vec{\mu}$) and parallax (π) measurements from *Gaia*’s DR2 (e.g., Monteiro & Dias 2019). Once the OCs are identified and cluster memberships are assessed, it is crucial to characterise the fundamental OC properties including t_{age} , $[\text{Fe}/\text{H}]$, the distance to the OC (D), and reddening (A_v). Usually, these studies use membership data from previous studies and characterise the OC properties (as an example of exception, Monteiro et al. 2017, assign memberships and find OC properties). The largest recent study directly adopting the CG-DR2 memberships was done by Bossini et al. (2019) using a Bayesian framework BASE9 (von Hippel et al. 2006; Jeffery et al. 2016). However, this work used fixed $[\text{Fe}/\text{H}]$ while determining the OC properties, either at the solar value or adopted from past constraints where available. Using *Gaia* DR2 data, Cantat-Gaudin et al. (2020, hereafter CG20) estimated global cluster properties such as t_{age} , A_v , and D . In a recent study, Hunt & Reffert (2023) used Hierarchical Density-Based Spatial Clustering of Applications with Noise (HDBSCAN) to identify clusters in *Gaia* DR3 data up to magnitude $G \sim 20$. Then, they verified these cluster members through a statistical density test and a CMD classifier based on a Bayesian neural network (BNN). In this way, they create one of the largest homogeneous catalogues of OC and their properties.

In this work, we present the first step of a systematic in-depth study of the rich ($N_{\text{cl}} > 500$) nearby ($D/\text{kpc} < 3$) OCs. We use *Gaia*’s DR3 to first ascertain membership and then constrain the fundamental properties using a Bayesian framework. In addition, we aim to reduce subjective human intervention in constraining the fundamental properties using isochrone fitting. Furthermore, we are interested in being able to identify exotic stellar members including BSs and WD binaries that do not fall into any well characterised sequence on the CMD in future work. This motivates us to combine

the rigors of the studies on specific OCs (e.g., Geller & Mathieu 2012) and the uniformity of analysis in automated OC surveys using ML methods (e.g., CG-DR2), where it is not easy to interpret the meaning of the membership statistic. Because of the extraordinary success of ML studies to identify OCs using *Gaia*’s DR2, we do not focus on identifying or finding OCs. Instead, here we embark on an in-depth study using *Gaia*’s DR3 (which provides significant improvements in systematics and astrometric solutions Gaia Collaboration et al. 2022) of rich nearby OCs already mentioned in the CG20 catalog.

While a vast body of past studies exists on this topic, our study is different from them with several key improvements and flexibility. We first identify the OC members and then with those members, we also estimate the clusters’ global properties. We use a new completely non-parametric approach in our analysis, both for membership assessment and estimation of OC properties, making no a-priori assumptions on any distributions for the field or cluster stars. Our method automatically takes into account highly correlated error matrices associated with the astrometric and photometric properties of individual stellar objects. Our method is able to handle OCs located in sparse as well as crowded fields and is able to extract membership probabilities even when the phase-space density of field stars starts becoming comparable (or even higher) than that of cluster stars. Once the members are identified, we estimate OC fundamental properties using a Bayesian framework with no subjective intervention. This is traditionally challenging because the MS on a CMD can show a spread due to photometric errors, A_v , and existence of stellar binaries. Thus, identifying the single MS and fitting an isochrone is usually not trivial without human supervision. We overcome this challenge.

The rest of the paper is organised as follows. In section 2 we describe the details of how we select the data. In section 3 we describe how we calculate the membership probabilities. In section 4 we describe how we constrain the fundamental properties of the OCs using the member stars. In section 5 we show our key results and conclude in section 6.

2. DATA SELECTION

We select 21 OCs from the CG20 catalog that are not within $\pm 5^\circ$ of the Galactic plane, has $N_{\text{cl}} > 500$ (as mentioned in CG20), and are within a distance $D/\text{kpc} < 3$. Although the methods we have developed can be applied to crowded as well as sparse fields, as a first application, we have chosen to be sufficiently away from the Galactic plane. While we select the target OCs based on *Gaia*’s DR2 used by CG20, we use DR3 data for our analysis. In DR3, on an average, the astrometric precision in π ($\vec{\mu}$) has increased by $\sim 30\%$ (\sim factor of 2). The systematic errors in astrometry are suppressed by 30–40% for π and by a factor of ~ 2.5 for $\vec{\mu}$. DR3 also provides bet-

ter precision in photometry with no systematics above $\sim 1\%$ in any bands G , BP , and RP (e.g., [Gaia Collaboration et al. 2016, 2022](#)). These improvements are expected to help ascertaining cluster membership and finding the cluster’s global properties.

For each of our selected OCs, we analyze *all Gaia* sources with $G < 18$ within a projected distance $r_{2D} = 20$ pc. Neither of these cuts are explicitly required in our analysis. We use the magnitude cut because fainter stars exhibit larger astrometric and photometric errors and we find that including them in the analysis does not give us any additional benefits in the evaluation of cluster properties. The cut on r_{2D} is essentially to limit the total number of *Gaia* sources we need to analyse, thus, computational cost. We find that in all our analysed OCs, the projected number densities of field stars become significantly higher than that of the OC members well below $r_{2D}/\text{pc} = 20$ (see [Appendix A](#) for more details). In comparison, $r_{2D}/\text{pc} = 20$ is $\gtrsim 3$ times the reported r_{50} , the radius containing 50% of the cluster members, reported in CG20 for all OCs we study.

In contrast to several earlier studies, we do not impose any cuts based on the Renormalised Unit Weight Error (RUWE) for the sources. While, $\text{RUWE} > 1.4$ may indicate an inadequate single star astrometric solution for a source, past studies indicate that the high RUWE is often obtained for stellar binaries ([Jorissen 2019; Belokurov et al. 2020](#)). Since, imposing an upper limit on RUWE may preferentially exclude stellar binaries, we choose not to impose a hard RUWE cut-off. Nevertheless, we take into account π and $\bar{\mu}$ errors for each source by using the three-dimensional Gaussian’s where the mean is given by the fiducial values for the source and the covariance matrix is constructed from the reported 1σ errors in *Gaia*-DR3. This allows us to, for example, put more weight on stars that have small errors in $\bar{\mu}$ and π .

3. MEMBERSHIP ANALYSIS

The OCs being part of the disk population of the MW, with low central stellar densities, clearly identifying cluster members through a combination of RA, Dec, π , and $\bar{\mu}$ poses challenges. The collection of stars to consider and contribution from the field increases with increasing r_{2D} . A small enough r_{2D} may allow identification of cluster stars with $\bar{\mu}$ significantly different from those in the field. However, in the crowded fields of the typical OCs, increasing r_{2D} may lead to such dominance of field stars that it becomes impossible to easily separate the cluster from the field even after considering π and $\bar{\mu}$. This difficulty usually limits the ability to consider stars with sufficiently large r_{2D} .

We develop a non-parametric method that can extend to arbitrarily large r_{2D} , the limitation coming only from the fact that the number of stars to analyse increases significantly with increasing r_{2D} . We calculate the clus-

ter membership probability

$$P_{\text{mem}} = \frac{P_{\text{cl}}}{P_{\text{cl}} + P_{\text{field}}}, \quad (1)$$

where P_{cl} (P_{field}) denotes the probability that a particular star belongs to the cluster (field). The calculation of P_{cl} and P_{field} is based on an initial guess taking into account the three-dimensional parameter space π , and $\bar{\mu}$. We do not assume any particular shape or symmetry for the distribution of the cluster stars. Moreover, this method can be applied to any star cluster independent of the crowding near its location, the certainty of membership automatically takes into account the effects of crowding. Below we describe how we calculate P_{field} and P_{cl} in detail.

3.1. Construction of the cluster’s probability density function

In order to evaluate P_{cl} for any particular star with a given $\{\mu_{\text{RA}}, \mu_{\text{dec}}, \pi\}$, we first need to construct a three-dimensional probability density function (PDF) for cluster stars, $f_{\text{cl}}(\mu_{\text{RA}}, \mu_{\text{dec}}, \pi)$. This presents a chicken-and-egg problem, since identifying cluster members requires some prior knowledge of the cluster itself. Thus, we are forced to take an initial guess of a collection of stars that, with very high probability, are cluster members with little chance of contamination from the field. Selecting the stars we can use as the initial guess of cluster stars is the only step in our analysis which requires human intervention.¹

Based on several trials, we have decided to analyze all stars with $r_{2D}/\text{pc} \leq 1$ to identify our initial guess of cluster stars by clustering of sources in $\{\mu_{\text{RA}}, \mu_{\text{dec}}, \pi\}$. [Figure 1](#) illustrates our strategy using a pair-wise three-step process for NGC 2287 as an example. First, we identify the clustered sources in $\{\mu_{\text{RA}}, \mu_{\text{dec}}\}$ (top panel, green circles). However, in $\{\mu_{\text{RA}}, \pi\}$, 4 out of these selected sources do not seem to be tightly clustered with the others. Hence, we discard these 4 sources from our selection and consider only the others (middle panel, blue plus). All sources clustered both in $\{\mu_{\text{RA}}, \mu_{\text{dec}}\}$ and $\{\mu_{\text{RA}}, \pi\}$ are then found to be clustered also in $\{\mu_{\text{dec}}, \pi\}$ (bottom panel, red dots) in this particular example. Thus, the red dots constitute the sources with $r_{2D}/\text{pc} < 1$ exhibiting tight clustering separate from the other stars in $\{\mu_{\text{RA}}, \mu_{\text{dec}}, \pi\}$. These sources constitute our initial guess of cluster stars for this OC. Note that these sources are simply our initial guess for cluster stars and it is important to be very selective because these stars would constitute f_{cl} . A cluster identification algorithm could remove the necessity for human intervention at this stage. However, we find that by eye we are able to be more selective in our choice, especially for OCs

¹ We have plans to improve this in future.

in relatively more crowded regions. Our tests suggest that including or excluding a small number of marginal sources does not influence the final P_{mem} of the much larger number of sources we ultimately analyse. Once our initial guess of cluster stars is selected, we proceed to construct f_{cl} . Instead of using the fiducial $\{\bar{\mu}, \pi\}$ values for the stars, we assume that the i th star is represented by a three-dimensional Gaussian \mathcal{N}_i with the mean given by the fiducial values and covariance matrix given by the correlated errors reported in *Gaia*'s DR3.² The cluster PDF is then $f_{\text{cl}} = \sum_i \mathcal{N}_i / N$, where N is the total number of sources in the initial guess. In practice, we randomly draw from \mathcal{N}_i 100 times for the i th star and combine all draws for all stars to construct f_{cl} using kernel density estimation (KDE) with Gaussian kernels from the Scipy package (Virtanen et al. 2020), bandwidth evaluated using Scott's method (Scott 2015). Thus, if the number of stars in our initial guess for cluster stars is N , f_{cl} is constructed with $100N$ points. Figure 2 shows f_{cl} for our example cluster NGC 2287 along with the initial guess of cluster stars.

3.2. Construction of the field PDF

Similar to the construction of f_{cl} , we construct f_{field} which gives a reasonable description of the field stars in $\{\bar{\mu}, \pi\}$. For this, we consider all stars within $r_{2\text{D}}/\text{pc} \leq 20$ except those that are very likely cluster members, i.e., stars with $\{\bar{\mu}, \pi\}$ within the volume containing 95% of the cluster PDF, f_{cl} . Using these stars, we construct f_{field} the same way as we construct f_{cl} . As an example, Figure 3 shows the histogram as well as the PDF for all stars with $r_{2\text{D}}/\text{pc} \leq 20$ (orange) for NGC-2287. It also shows the subset of stars except those within the volume containing 95% of total probability of f_{cl} (green). The tiny over-densities (visible only in the zoomed-in insets) is the contribution of the star cluster. Figure 3 illustrates a serious challenge in identifying OC members. Even for our example OC NGC-2287, which is relatively rich with stars, and even after considering all of the three relevant parameters, μ_{RA} , μ_{dec} , π , the contribution from the OC is rather small compared to those in the field if a reasonably large $r_{2\text{D}}/\text{pc} \leq 20$ is considered. This challenge often limits the $r_{2\text{D}}$ up to which stars can be analyzed. In our strategy, we are not limited by this challenge, since after f_{cl} and f_{field} are constructed, we can easily evaluate the membership probability of any star at any $r_{2\text{D}}$. For us, the limit comes from practical considerations and computational cost since the number of stars to analyse increases linearly with $r_{2\text{D}}$.

3.3. Cluster Membership probabilities

Once f_{cl} and f_{field} are constructed, it is straightforward to calculate the probability of drawing a particular

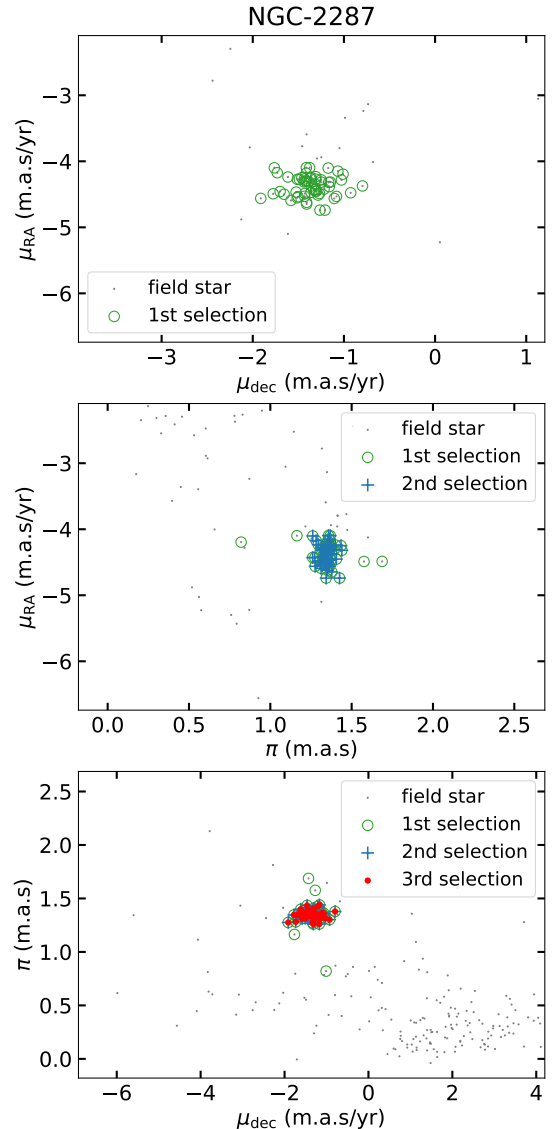


Figure 1. Illustration of how we select the initial guess for cluster member sources using NGC 2287. We first select all sources with $r_{\text{proj}}/\text{pc} \leq 1$. We identify all sources closely clustered in the μ_{RA} and μ_{dec} plane (top panel, green circles). We then check these sources in the $\mu_{\text{RA}}-\pi$ plane $\pi-\mu_{\text{dec}}$ planes and discard those that are not closely clustered. For example, in the middle panel we discard four sources (green open circles) and only select the others (blue '+' with green open circle). In the bottom panel we find that the sources closely clustered both in the $\mu_{\text{RA}}-\mu_{\text{dec}}$ and $\pi-\mu_{\text{RA}}$ planes are also closely clustered in $\mu_{\text{dec}}-\pi$ (green circles with blue '+' and red dot). Sources depicted by the green circles, blue '+', as well as red dot constitute our initial guess for cluster members. Grey dots denote other stars that show no clustering.

² If the detailed posteriors for each star were available, we could have used those. In the absence of this, we have to adopt the normal distribution.

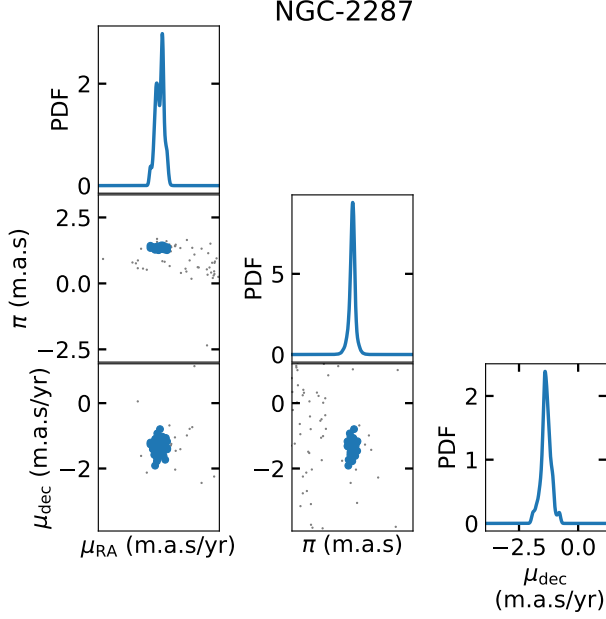


Figure 2. PDFs for the sources in our initial guess of cluster members (blue dots). Grey dots denote all other sources with $r_{\text{proj}}/\text{pc} \leq 1$.

star from either the cluster or the field PDF. We take into account errors in $\{\mu_{\text{RA}}, \mu_{\text{dec}}, \pi\}$ measurements for each star in the same way as described above. We draw 100 points from a 3D gaussian created using the fiducial values as mean and the errors as 1σ covariance. For each of these values, we calculate the probability densities corresponding to the PDF f_{cl} (f_{field}) and take the average to finally arrive at the probability P_{cl} (P_{field}) of drawing this particular star from f_{cl} (f_{field}). Incorporating the astrometric errors instead of simply using the fiducial values allows us to directly factor in accuracy of astrometric measurements of each star into the final uncertainties in determining P_{cl} .³ We evaluate P_{cl} and P_{field} for all stars with $r_{2\text{D}}/\text{pc} \leq 20$ for each OC and calculate the membership probability (P_{mem}) using Equation 1. Figure 4 shows star count as a function of P_{mem} for our example OC NGC-2287. The distribution shows two clear peaks populated by high-probability cluster stars and those that clearly do not belong to

³ For example, consider stars 1 and 2, both with fiducial values of $\bar{\mu}$ and π close to that of the cluster's, but the former has larger errors than the latter. Using our strategy, P_{cl} for the former will automatically be higher than that of the latter. In contrast, among two stars, both with fiducial values of $\{\mu_{\text{RA}}, \mu_{\text{dec}}, \pi\}$ far away from the peak of f_{cl} , the one with larger errors will likely have a higher P_{cl} because the long tails will allow higher overlap with f_{cl} . Fainter stars typically have larger astrometric errors. Incorporating correlated astrometric errors directly into the analysis also takes that into account.

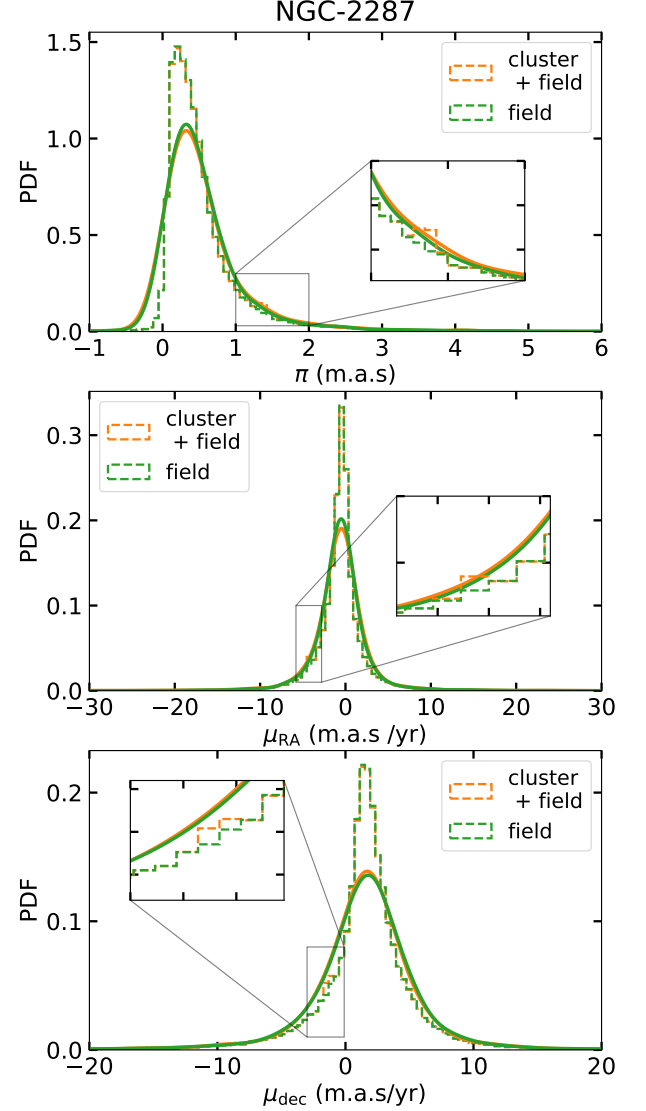


Figure 3. Normalized histogram (dashed) and PDF (solid) for sources within $r_{\text{proj}}/\text{pc} \leq 20$ from the cluster center of NGC-2287. Green and orange denote all sources and those excluding our initial guess of cluster members (detailed discussion in section 3 and in Figure 1). Top, middle, and bottom panels are for π , μ_{RA} , and μ_{dec} , respectively.

the cluster. There is a low floor in star count in between the two extreme P_{mem} values corresponding to the cluster members and non-members. In order to find the optimal cut-off value in the membership probability, $P_{\text{mem},c}$, we first estimate the average level of the flat part, $n_{\text{ref}} = \Delta N / \Delta P_{\text{mem}}$, where, ΔN is the total number of stars within $\Delta P_{\text{mem}} = 0.8 - 0.5$. We define $P_{\text{mem},c}$ as the P_{mem} value above which $\delta N / \delta P_{\text{mem}} > 5n_{\text{ref}}$ and increases monotonically, where δ denotes bin-wise values. We consider all stars with $P_{\text{mem}} > P_{\text{mem},c}$ as clus-

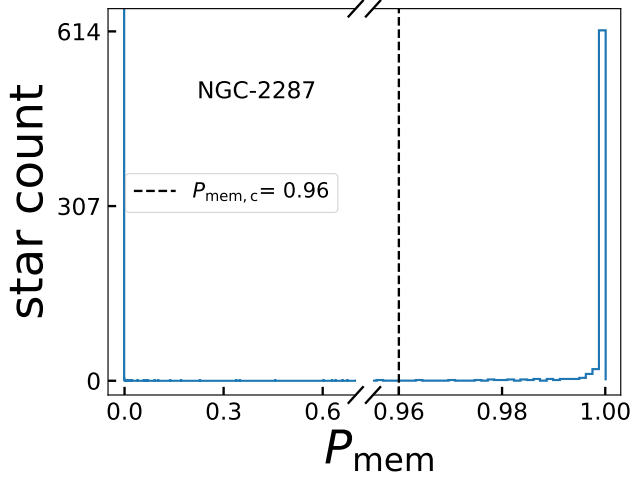


Figure 4. Source count as a function of membership probability P_{mem} . Sources with very low P_{mem} clearly belong to the field. Sources count increases sharply near $P_{\text{mem}} \approx 1$. The dashed black vertical line denotes the cut-off value $P_{\text{mem},c}$ in P_{mem} for this cluster. Very few sources have $P_{\text{mem}} < P_{\text{mem},c}$ until $P_{\text{mem}} \sim 0.0$. Thus, our evaluated P_{mem} divides the sources in two clearly distinct groups, cluster members with $P_{\text{mem}} \approx 1$ and non-members with $P_{\text{mem}} \approx 0$.

ter members.⁴ In Figure 5 we show the CMD (bottom) and $\bar{\mu}$ vs π (top) for all stars with $r_{2D}/\text{pc} \leq 20$ of NGC-2287. The grey dots denote all stars we analyse, the coloured dots denote cluster members based on $P_{\text{mem},c}$ described above. The colour bar denotes P_{mem} . Clearly, stars near the cluster center in $\{\bar{\mu}, \pi\}$ have very high P_{mem} , while P_{mem} gradually decreases towards the outskirts. Also note that P_{mem} decreases faster towards the $\{\bar{\mu}, \pi\}$ with a higher field star density due to higher contamination. These are all expected and desirable behaviours. In Figure 6, we compare μ_{RA} , μ_{dec} , and π for our initial guess (orange) and final (blue) cluster members for NGC-2287 as an example. The histograms show the one-dimensional distributions and dots denote the sources. Grey dots denote sources that are not members of NGC-2287. We also show the CMD and show the relative positions of our initial guess and final clusters members. The excellent alignment in parameter space between the initial guess and final cluster members illustrates the validity of our initial guess and the overall strategy to identify cluster members. Also note that the sources that constitute our initial guess for f_{cl} , span the entire range of the CMD indicating that our choice of sources were not biased.

⁴ The exact cut-off, $P_{\text{mem},c}$, is a matter of choice. One may choose to be more or less selective. We make public P_{mem} for all stars to enable users to freely choose a different cut-off if desired.

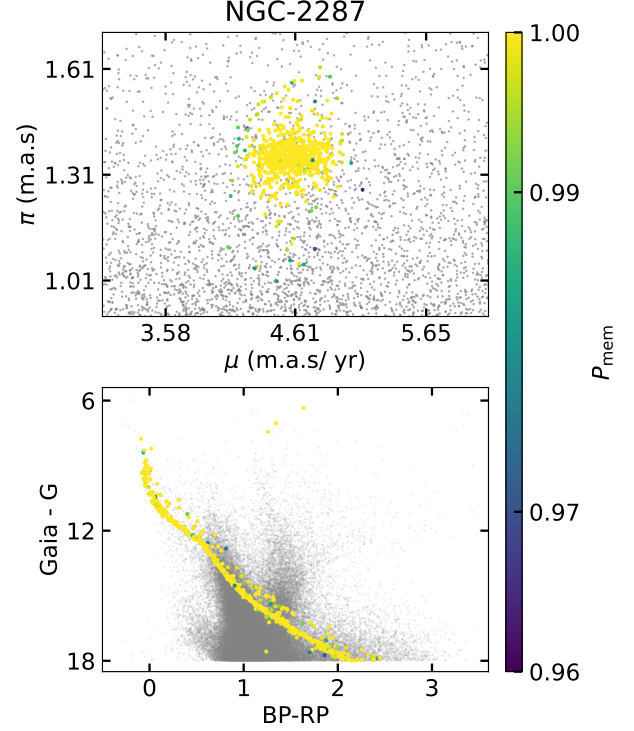


Figure 5. All sources with $r_{\text{proj}}/\text{pc} \leq 20$ for NGC 2287. Colored dots denote sources with $P_{\text{mem}} > P_{\text{mem},c}$, i.e., sources we identify as cluster members, where the color denotes P_{mem} . Sources denoted by grey dots have $P_{\text{mem}} < P_{\text{mem},c}$. *Top*: π and $\bar{\mu}$ of all cluster members (colored dots) and non-members (grey dots). *Bottom*: CMD for all sources. Clearly, the cluster members produce a very clean CMD. We find a few giant star with very high P_{mem} . Also, as expected, fainter stars have typically lower P_{mem} .

4. ESTIMATION OF CLUSTER PROPERTIES

Once the cluster members are selected, we can estimate the cluster global properties. We re-calculate the astrometric properties, μ_{RA} , μ_{dec} , and π of the clusters. For each cluster, we use *Gaia* DR3's estimated values and associated errors for each cluster member and adopt one-dimensional Gaussians. We add these Gaussians to find the overall PDF. We fit this PDF with a Gaussian to estimate the overall astrometric properties of the cluster. Our estimates of μ_{RA} , μ_{dec} , and π for each cluster are given in Table 1.

Using the cluster members we estimate cluster properties such as t_{age} , $[\text{Fe}/\text{H}]$, D , and A_v in a Bayesian framework. In literature, often cluster parameters are estimated using isochrone fitting of the cluster CMD by varying t_{age} , $[\text{Fe}/\text{H}]$, D , and A_v through visual inspection introducing subjectivity. In contrast, our method uses a robust Bayesian framework to estimate the posterior distributions of these parameters using isochrone

NGC-2287

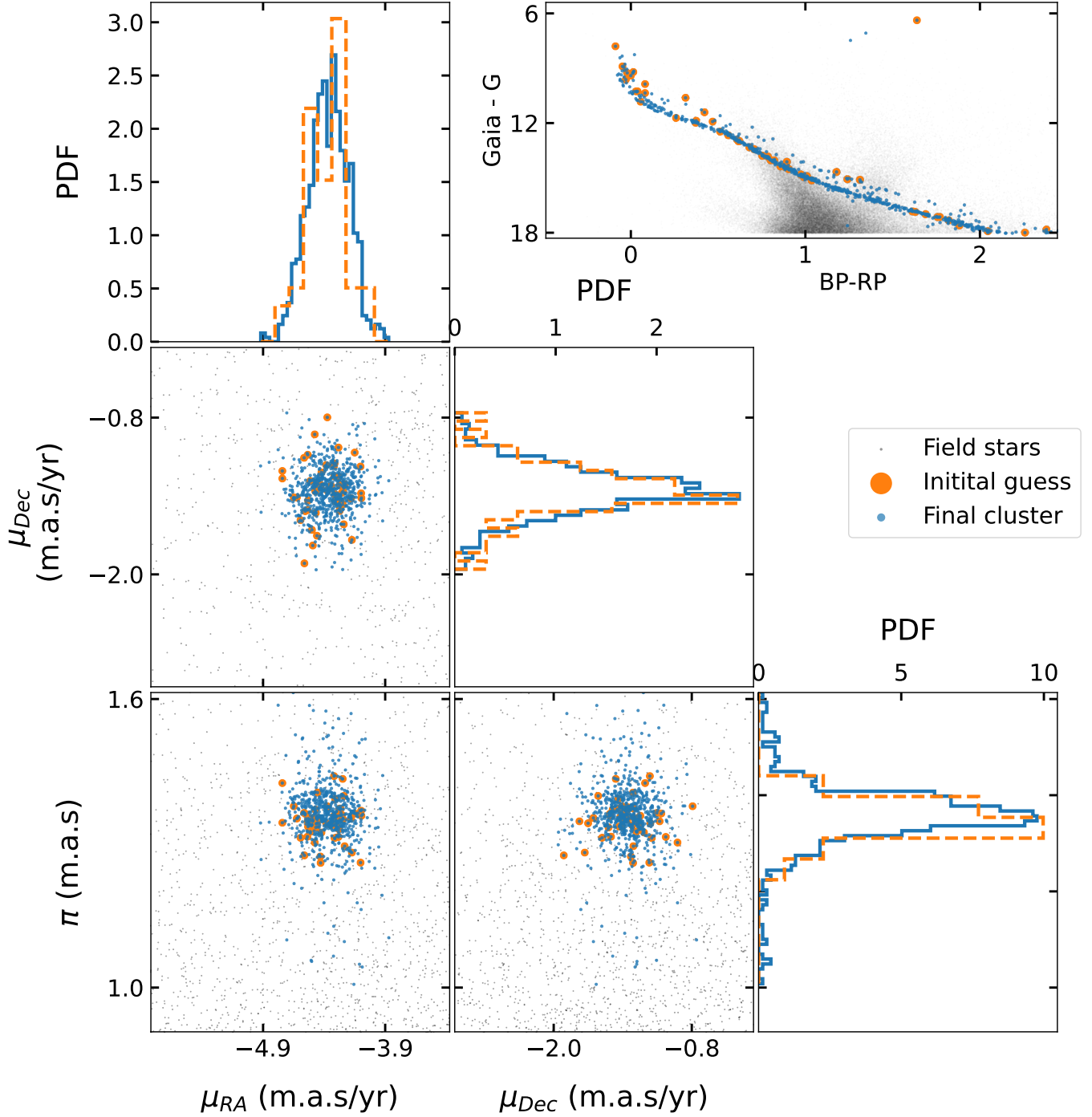


Figure 6. The PDFs and scatter plots for our initial guess (orange) and final identified (blue) cluster members in $\{\vec{\mu}, \pi\}$ for NGC 2287. In the top right corner, we show the CMD. Grey dots denote non-members.

fitting and requires no visual inspection. As a result, the same technique can be uniformly used for all clusters. Below we discuss the detailed procedure.

4.1. Identification of the single-star main sequence

The primary challenge in fitting an isochrone to a CMD without any visual inspection is in the identification of the single-star MS. The presence of unresolved binaries as well as photometric errors, which also often depends on the magnitude, create a spread in the CMD of a star cluster. While it is straightforward to visually understand where the single-star main sequence is on the CMD, it isn't so without visual inspection. Below we explain the technique we have developed that can be used self-consistently for any cluster.

It is expected that the total binary fraction in an OC is $\lesssim 50\%$ for GKM stars (Jadhav et al. 2021). This means that for any given range in magnitude, the highest density of sources on the CMD should correspond to the single-star main sequence. On the other hand, while the individual photometric errors can be large, they are expected to be random and centred around the actual value. Hence, while photometric errors can spread the single-star MS, if the colors and magnitudes for each source are treated as a distribution considering the fiducial values and associated errors, the source density is expected to remain roughly near the correct location provided there are enough sources to consider.

We exploit the above expectations in the following way. We first sort the MS stars in G. Then from the top of the MS, we take a sliding window of 30 sources and create a two-dimensional PDF in G and BP-RP using the reported fiducial values and associated errors in *Gaia*'s DR3 assuming Gaussian distributions for each source.⁵ We find the location of the dominant mode of the PDF for each group. In rare occasions, if we find two modes of roughly equal importance, we choose the mode at the lower BP-RP since the other mode is expected to come from stellar binaries. For all sources, we find that DR3's errors in BP-RP are significantly higher compared to that in G. Hence, we adopt the 99th percentile value in the errors in BP-RP for all sources in the corresponding group as a conservative estimate for the error in the location of the mode. At the end of this exercise, we obtain the mode locations and associated errors for all sources within small slices in G across the whole CMD of the OC.

We fit a degree-5 polynomial through the mode locations on the CMD. We use this best-fit polynomial to define the locus of the single-star MS on the CMD. Us-

⁵ We have tested by varying the size of this sliding window. Choosing a large number reduces resolution at the top of the MS near the turn-off region. On the other hand, choosing too small a number increases fluctuations significantly. We find that the adopted size provides the most optimal outcome for the OCs we have considered.

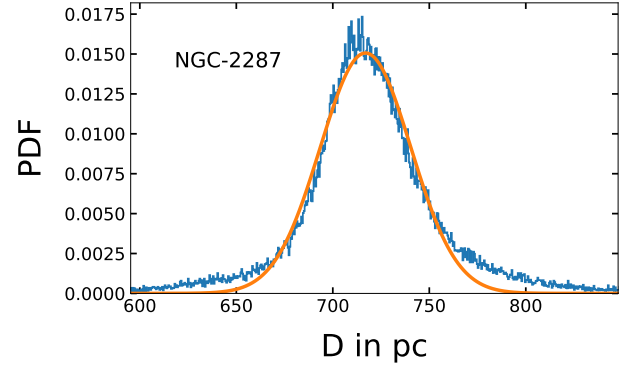


Figure 7. We estimate each cluster member's distance by cross-matching the data with Bailer-Jones et al. (2021). The blue histogram shows the distance distribution of the cluster members we identify for NGC 2287 taking into account estimate errors in the distance. The orange line shows the best-fit Gaussian to the distance distribution which we use as a prior to our estimation for the cluster's distance.

ing the associated errors in the locations of the modes, we fit two separate degree-5 polynomials depicting the spread below and above the single-star MS.

4.2. Parameter estimation

We use the publicly available Markov-Chain Monte Carlo (MCMC) toolkit *emcee* (Foreman-Mackey et al. 2013) to perform parameter estimation for each OC we analyse. In all cases, we use 128 walkers initially distributed according to the prior distributions. We perform 60,000 steps using the Metropolis-Hastings algorithm. We discard the first 30,000 steps as burn-in and trim the later steps by choosing 1 position in every 15 steps. We have tested for convergence in the posterior distributions and find that they converge well before 40,000 steps adopting the same burn-in and trimming (see Appendix B and Figure 14 for more details). We have also tested varying $P_{\text{mem},c}$ and find that the posteriors remain statistically identical (see Appendix C and Figure 15 for more details).

4.2.1. Source sampling

In most of our clusters, the giant branch is not populated well enough. In general, t_{age} estimation from isochrone fitting using the giant branch can be tricky due to the rapid evolution of stars in the giant phase. Hence, we use up to the MS turn-off region to estimate the cluster properties. Within the MS, the brighter the source, the lower the photometric errors (Lindegren et al. 2018). On the other hand, as the magnitude decreases, the number of sources decrease fast because of the stellar mass function. As a result, if the actual observed sources, for example, within the single-star MS

strip (subsection 4.1), are sampled directly, the faint part of the CMD, populated by a large number of sources with high photometric errors, would receive a lot more weight in the calculation of likelihood and the MS turn-off region would receive very little weight. As a result, the likelihood calculation would become less sensitive to the MS turn-off region which usually has the most constraining power in determining the t_{age} of the cluster.

We overcome these challenges by uniformly sampling 1000 *Gaia*-G values between magnitudes corresponding to the MS turn-off and $G=18$ for each OC. For each of these G values, we uniformly sample BP-RP within the range obtained from the spread we estimate for the single-star MS. These $\{G, \text{BP-RP}\}$ points represent our data for the single-star MS which we will denote as \vec{d} .

4.2.2. Construction of likelihood

For each cluster, the parameters we want to estimate are t_{age} , $[\text{Fe}/\text{H}]$, D , and A_v , which we collectively denote as $\vec{\theta} \equiv \{t_{\text{age}}, [\text{Fe}/\text{H}], D, A_v\}$. We generate isochrone models using the MIST isochrone package (Dotter 2016; Choi et al. 2016). While each isochrone in MIST takes t_{age} , $[\text{Fe}/\text{H}]$, and A_v as input, the distance D is used to convert the absolute magnitudes generated by MIST (Dotter 2016; Choi et al. 2016) to apparent magnitudes available in *Gaia*'s DR3.

We define the likelihood function (\mathcal{L}) as-

$$\ln \mathcal{L} = P(\vec{d}|M; \vec{\theta}) = -\frac{1}{2} \sum_i \left[-\frac{(d_i - M_i(\vec{\theta}))^2}{s_i^2} + \ln(2\pi s_i^2) \right] \quad (2)$$

where, the subscript i denotes the index of the data points, M_i denotes the point on CMD given by MIST's model isochrones with parameters $\vec{\theta}$.

$$s_i^2 = \sigma_i^2 + f^2, \quad (3)$$

where, σ_i is the error at d_i estimated in subsection 4.1. and f is an ad hoc numerical parameter, not associated with anything physical, introduced to stabilize the likelihood function (for a detailed discussion, see Foreman-Mackey et al. 2013).

Using the above likelihood function we proceed to evaluate the posterior distribution of $\vec{\theta}$. The posterior is defined as-

$$P(\vec{\theta}|\vec{d}, \vec{\sigma}; M) = P(\vec{d}|\vec{\theta}, \vec{\sigma}; M)P(\vec{\theta}). \quad (4)$$

where $P(\vec{\theta})$ denotes the prior distribution.

4.2.3. Construction of priors

We use flat priors in t_{age} , $[\text{Fe}/\text{H}]$, and A_v in the range 10^7 – 10^{10} yr, -1.0 – 0.5 , and 0 – 5 magnitudes, respectively.

The most straightforward way to estimate D could have been inversion of π given in *Gaia*'s DR3. However, estimation of D , especially for stars fainter than

$G = 17$, via direct inversion of π can introduce large errors due to uncertainties in *Gaia*'s π measurement. Moreover, direct inversion of negative π is just incorrect. Instead, Bailer-Jones et al. (2021) implemented a Bayesian approach taking into account interstellar extinction, color, and magnitude to determine the posteriors for what they called the *photogeometric* distance from π . We cross-match the individual cluster members to the Bailer-Jones et al. (2021) catalog using RA-dec and cross-match radius $< 1''$. We find that this choice of cross-match radius does not create multiple matches due to crowding in the clusters we have studied. Once we identify the sources in the catalog, we collect the median, 16th and 84th percentiles of the photogeometric distance posteriors given by Bailer-Jones et al. (2021). For each cluster member, we approximate the photogeometric distance posterior as a Gaussian based on the median, 16th and 84th percentiles. We combine these to find the overall PDF. We then find the best-fit Gaussian for this combined PDF. This best-fit Gaussian is used as the prior distribution for D .

Figure 8 shows the posterior distributions for D , $[\text{Fe}/\text{H}]$, A_v , and t_{age} for our example OC NGC-2287. The three contours in the two-dimensional joint posterior distributions enclose 68%, 90%, and 95% of the marginalised probability. The vertical dashed lines in the one-dimensional marginalised distributions from left to right show the 16, 50, and 84 percentiles. Top right panel shows the CMD for the cluster members (blue dots). We show the reference single-star MS identified using modes for the distribution of sources on the CMD (black dashed; subsection 4.1) and the model isochrone created using MIST using the median of the posterior distribution of $\vec{\theta}$ (red solid). Clearly, our estimated parameters provide a good fit to the CMD. Interestingly, although the giant region was not considered in \vec{d} , the model isochrone fits the few giants present in NGC-2287 too. Also note that the model isochrone deviates from the reference single-star MS for $G \gtrsim 17$. This is partially due to the relatively higher photometric errors for fainter sources. The under-prediction of magnitudes for stars in the mass range 0.25 to $0.85 M_{\odot}$ by MIST isochrones may be also related to its limitations in the convection prescription (Brandner et al. 2023).

5. RESULTS AND DISCUSSION

We have summarised all estimated properties for the 21 OCs in Table 1. For each OC, we have listed the number of cluster members according to our analysis. We also report the median and the spread between the 16th and 84th percentiles for the astrometric and cluster properties for each OC. Overall, the OCs in our sample exhibit a reasonably large range in properties. The number of cluster members N_{cl} varies from 570 for NGC-2539 to 2830 for NGC-7789 with a median $N_{\text{cl}} = 884$.

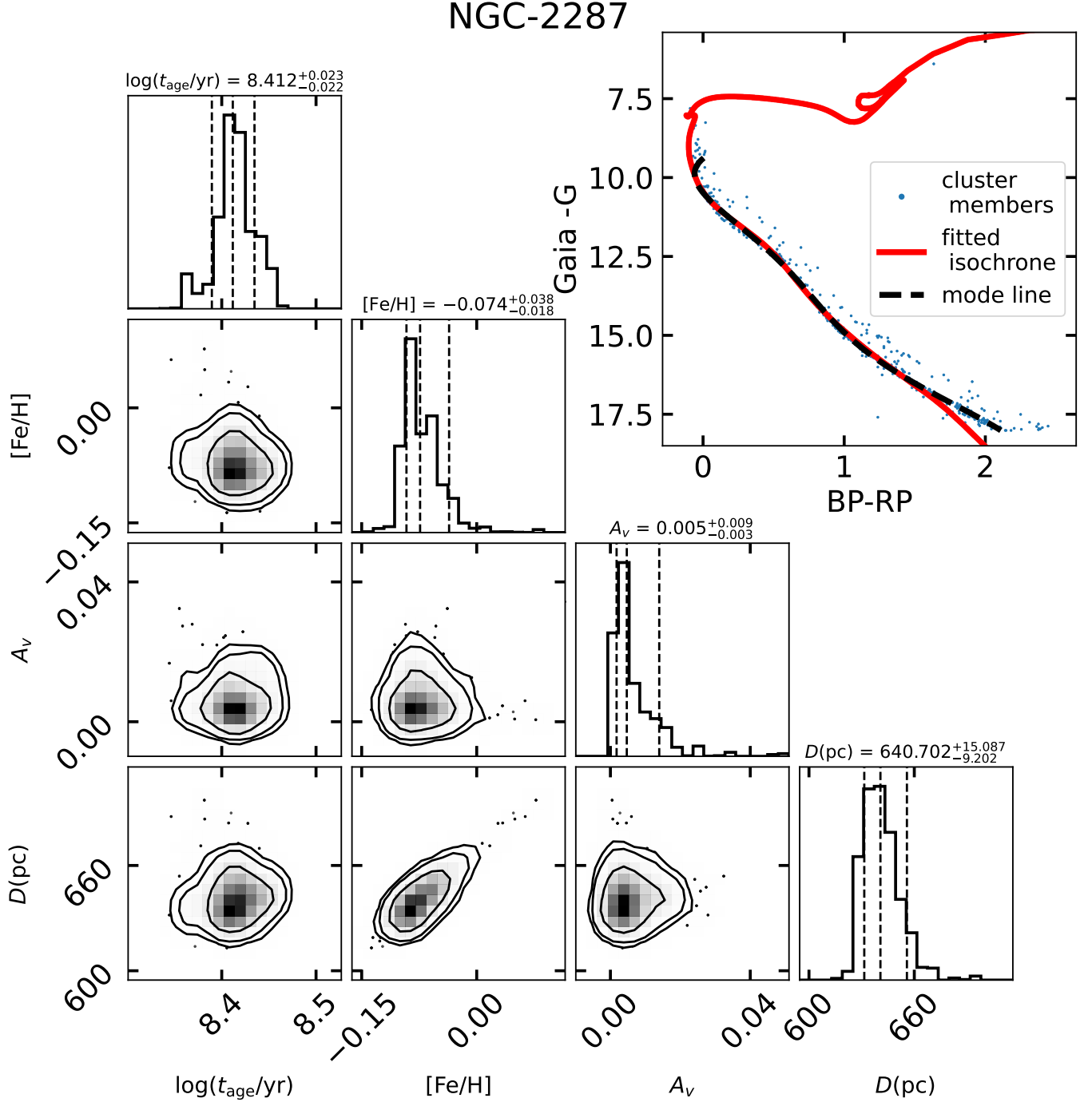


Figure 8. Corner plot showing two-dimensional joint and one-dimensional marginalized posterior distributions for NGC-2287 cluster properties. The contours in the two-dimensional joint posterior distributions enclose 68%, 90%, and 95% probabilities. The vertical lines in the one-dimensional posterior distributions show the median, and 16% and 84% confidence bounds. We show the CMD in the right top corner. Dots represent cluster members, i.e., sources with $P_{\text{mem}} > P_{\text{mem,c}}$. The black dashed and the red solid lines denote the best-fit line connecting the modes (see details in [subsection 4.1](#)) and the best-fit isochrone created using the median values from the posterior distributions, respectively. Clearly, the isochrone is a very good fit for the CMD except near very low- G sources where *Gaia*'s photometry has large errors.

Table 1. Global properties of all the clusters.

Cluster	N_{cl}	$N_{\text{cl,CG20}}$	$\log(t_{\text{age}}/\text{yr})$	[Fe/H]	Extinction	D	D	μ_{RA}	μ_{dec}	π	$r_{2\text{D}}^*$
Name	($P_{\text{mem,c}}$)	($P_{\text{mem,CG20}} > 0.7$)	Posteriors from Bayesian parameter estimation				prior				
			(dex)	(dex)	(mag)	(pc)	(pc)	(m.a.s/yr)	(m.a.s/yr)	(m.a.s)	(pc)
Collinder-261	1910(0.93)	1799	$9.666^{+0.036}_{-0.027}$	$-0.486^{+0.115}_{-0.089}$	$1.438^{+0.057}_{-0.068}$	2633^{+54}_{-65}	2636 ± 471	-6.499 ± 0.084	-2.584 ± 0.086	0.229 ± 0.091	3
Collinder-69	787(0.90)	620	$6.502^{+0.002}_{-0.001}$	$0.019^{+0.008}_{-0.007}$	$0.248^{+0.048}_{-0.043}$	395^{+3}_{-2}	392 ± 14	0.628 ± 0.051	-1.833 ± 0.039	2.495 ± 0.047	1
IC-4651	1360.0(0.97)	806	$9.239^{+0.006}_{-0.006}$	$0.315^{+0.040}_{-0.036}$	$0.190^{+0.028}_{-0.032}$	907^{+4}_{-5}	911 ± 43	-2.430 ± 0.014	-5.190 ± 0.020	1.061 ± 0.020	< 1
Melotte-101	810(0.95)	472 [†]	$7.436^{+0.010}_{-0.012}$	$-0.252^{+0.022}_{-0.029}$	$1.326^{+0.005}_{-0.007}$	1727^{+21}_{-23}	2026 ± 186	-6.311 ± 0.010	3.532 ± 0.011	0.449 ± 0.011	1
Melotte-20	583(0.94)	747	$7.452^{+0.021}_{-0.021}$	$0.041^{+0.018}_{-0.018}$	$0.589^{+0.027}_{-0.027}$	180^{+3}_{-3}	172 ± 5	23.030 ± 0.072	-27.547 ± 0.057	5.902 ± 0.064	4
Melotte-22	1269(0.95)	952	$7.449^{+0.046}_{-0.030}$	$-0.076^{+0.083}_{-0.035}$	$0.659^{+0.036}_{-0.041}$	150^{+1}_{-3}	134 ± 3	20.986 ± 0.194	-47.463 ± 0.128	7.385 ± 0.135	5
NGC-1039	711(0.94)	555	$7.689^{+0.041}_{-0.005}$	$0.140^{+0.017}_{-0.020}$	$0.278^{+0.018}_{-0.009}$	533^{+7}_{-7}	488 ± 16	1.523 ± 0.067	-5.970 ± 0.064	1.836 ± 0.049	2
NGC-1647	688(0.94)	604	$7.839^{+0.031}_{-0.013}$	$0.112^{+0.030}_{-0.030}$	$1.308^{+0.009}_{-0.007}$	520^{+8}_{-9}	575 ± 19	-0.591 ± 0.370	-1.223 ± 0.241	1.241 ± 0.286	2
NGC-188	905(0.95)	857	$9.867^{+0.012}_{-0.011}$	$0.200^{+0.035}_{-0.051}$	$0.146^{+0.037}_{-0.030}$	1746^{+12}_{-16}	1792 ± 135	-2.212 ± 0.037	-1.266 ± 0.048	0.503 ± 0.041	7
NGC-2112	867(0.95)	687	$9.522^{+0.006}_{-0.006}$	$-0.441^{+0.022}_{-0.026}$	$2.258^{+0.013}_{-0.014}$	778^{+9}_{-8}	1042 ± 77	-2.854 ± 0.040	4.556 ± 0.032	0.836 ± 0.034	3
NGC-2287	679(0.96)	625	$8.412^{+0.023}_{-0.022}$	$-0.074^{+0.038}_{-0.018}$	$0.005^{+0.009}_{-0.003}$	640^{+15}_{-9}	716 ± 23	-4.351 ± 0.047	-1.290 ± 0.068	1.384 ± 0.104	3
NGC-2477	2696(0.94)	1713	$8.950^{+0.007}_{-0.008}$	$0.072^{+0.010}_{-0.008}$	$1.024^{+0.015}_{-0.013}$	1262^{+14}_{-14}	1384 ± 65	-2.556 ± 0.015	1.159 ± 0.023	0.881 ± 0.017	4
NGC-2516	1874(0.95)	652	$8.325^{+0.034}_{-0.050}$	$0.227^{+0.080}_{-0.050}$	$0.221^{+0.021}_{-0.021}$	414^{+19}_{-12}	406 ± 8	-5.775 ± 0.102	11.384 ± 0.113	2.411 ± 0.104	< 1
NGC-2539	570(0.96)	485 [†]	$8.857^{+0.011}_{-0.010}$	$-0.059^{+0.020}_{-0.027}$	$0.191^{+0.012}_{-0.012}$	1175^{+16}_{-17}	1252 ± 69	-2.236 ± 0.052	-0.599 ± 0.030	0.975 ± 0.061	2
NGC-2632	730(0.93)	685	$8.808^{+0.020}_{-0.014}$	$0.267^{+0.007}_{-0.006}$	$0.004^{+0.005}_{-0.003}$	173^{+1}_{-3}	183 ± 3	-35.325 ± 0.106	-12.697 ± 0.066	5.025 ± 0.095	5
NGC-2682	1178(0.93)	598	$9.752^{+0.004}_{-0.004}$	$0.088^{+0.006}_{-0.008}$	$0.003^{+0.004}_{-0.002}$	788^{+2}_{-4}	835 ± 34	-10.713 ± 0.020	-2.894 ± 0.021	1.108 ± 0.026	6
NGC-6124	1501(0.95)	1273	$8.481^{+0.009}_{-0.011}$	$0.134^{+0.017}_{-0.013}$	$2.116^{+0.008}_{-0.007}$	501^{+5}_{-3}	612 ± 23	0.196 ± 0.132	-2.281 ± 0.142	1.704 ± 0.171	1
NGC-6819	1689(0.95)	1527	$9.634^{+0.024}_{-0.818}$	$-0.536^{+0.045}_{-0.935}$	$0.683^{+1.345}_{-0.033}$	2027^{+63}_{-33}	2464 ± 268	-2.886 ± 0.018	-3.970 ± 0.018	0.370 ± 0.019	4
NGC-6939	821(0.96)	636	$9.471^{+0.005}_{-0.007}$	$-0.842^{+0.014}_{-0.014}$	$1.567^{+0.009}_{-0.010}$	1421^{+1}_{-1}	1803 ± 124	-1.883 ± 0.030	-5.309 ± 0.032	0.540 ± 0.027	3
NGC-6940	897(0.95)	572	$8.894^{+0.017}_{-0.022}$	$0.025^{+0.041}_{-0.041}$	$0.830^{+0.023}_{-0.022}$	1061^{+36}_{-25}	1011 ± 42	-2.401 ± 0.064	-9.559 ± 0.093	0.426 ± 0.084	< 1
NGC-7789	2830(0.92)	2830	$9.605^{+0.012}_{-0.007}$	$-0.742^{+0.028}_{-0.016}$	$1.001^{+0.015}_{-0.017}$	1420^{+13}_{-16}	1949 ± 163	-0.699 ± 0.039	-1.846 ± 0.044	0.550 ± 0.041	4

NOTE— Cluster properties including t_{age} , [Fe/H], D , A_v , μ_{RA} , μ_{dec} , π , $r_{2\text{D}}^*$, and N_{cl} for the 21 OCs we have studied. $r_{2\text{D}}^*$ is the r_{proj} where the surface density of cluster members $\Sigma_{\text{cluster}} = \Sigma_{\text{field}}^{\text{avg}}$, the average surface density of all sources with $15 \leq r_{\text{proj}}/\text{pc} \leq 20$. For comparison, we also show $N_{\text{cl,CG20}}$, the number of cluster members identified by CG20 with probability > 0.7 . The central value and the errors for each property denote the median, and 16% and 84% credible intervals. In most OCs we find significantly higher member numbers compared to those identified in CG20 (see discussion in [subsection 5.1](#)). Although, CG20 estimated fewer than 500 members for Melotte-101 and NGC-2539, we have analyzed these OCs and find $N_{\text{cl}} > 500$ (marked by [†]).

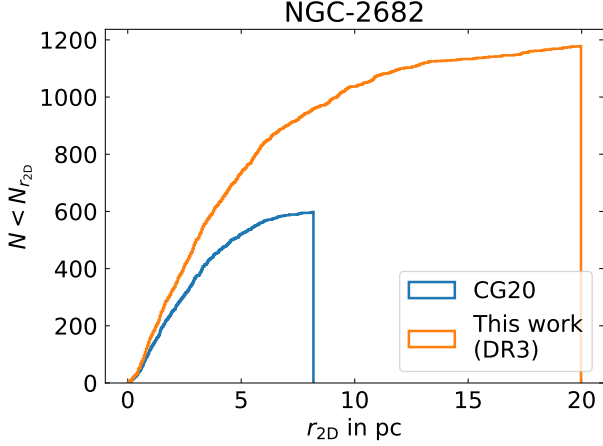


Figure 9. Cumulative member count as a function of r_{proj} for NGC 2682 as an example. Orange and blue denotes the cumulative member counts from our analysis using *Gaia*'s DR3 and those from CG20 using *Gaia*'s DR2. We not only identify more members at higher distances from the fiducial cluster center, we also identify more members compared to those identified by CG20 even within $r_{\text{proj}}/\text{pc} < 8$ where they analyzed.

These clusters are estimated to be as young as $t_{\text{age}} = 10$ Myr (for Collinder 69) to as old as $t_{\text{age}} = 7$ Gyr (for NGC-188) with a median at $t_{\text{age}} = 724$ Myr (for NGC-2539). The most distant and the closest OCs among the 21 are Collinder-261 at $D/\text{pc} \approx 2.7 \times 10^3$ and Mellotte 22 at $D/\text{pc} \approx 1.5 \times 10^2$. Our clusters exhibit a range $-0.84 \leq [\text{Fe}/\text{H}] \leq 0.31$ spanning both sides of the solar metallicity. We estimate that A_v ranges from 0.003 to 2.26 with a median at 0.59.

5.1. Number of cluster members

The cluster members we find can be directly compared with those mentioned in CG20 with some caveats. There are several key differences between these two studies. For example, we have used data from *Gaia*'s DR3, while CG20 used that from DR2. The meaning and method of estimating P_{mem} are also very different between these studies, as a result, a meaningful comparison cannot adopt the same $P_{\text{mem},c}$ used in these studies. Instead, we compare our membership numbers with those reported in CG20 (Table 1). We find that in 19 out of 21 clusters we have studied, the cluster member N_{cl} identified by us is higher than that in CG20 ($N_{\text{cl},\text{CG20}}$). We find that the median of $N_{\text{cl}}/N_{\text{cl},\text{CG20}}$ using $P_{\text{mem},\text{CG20}} > 0.7$ (0.5) is ≈ 1.3 (1.2), whereas, the largest (smallest) $N_{\text{cl}}/N_{\text{cl},\text{CG20}} \approx 2.9$ (0.8) for NGC-2516 (Mellotte-20) adopting $P_{\text{mem},\text{CG20}} > 0.7$.

A detailed analysis sheds light on the potential reasons for these differences. One possible source of this difference could have been the difference in the considered

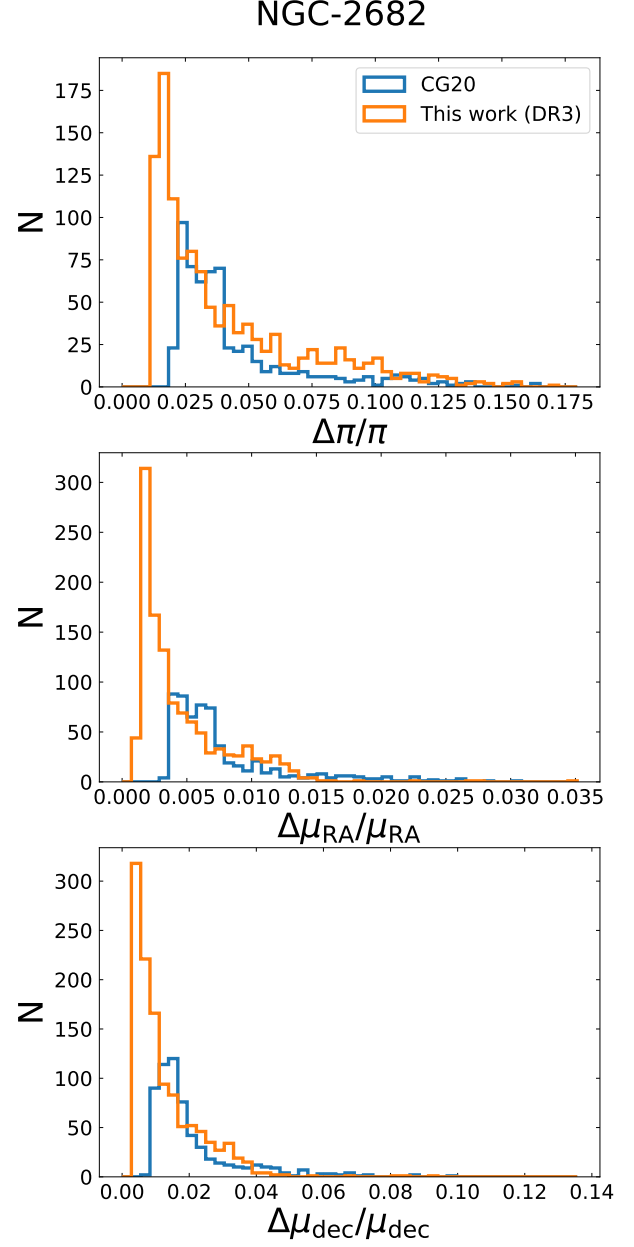


Figure 10. Histograms of relative errors in π (top), μ_{RA} (middle), and μ_{dec} (bottom) for the cluster members we identify using *Gaia*'s DR3 (orange) and those identified by CG20 (blue). The shift in the peak of the distributions towards lower errors in our analysis is due to the improvement of astrometric measurements in *Gaia*'s DR3.

limiting r_{2D} . As an example, we show the cumulative source count as a function of r_{2D} in Figure 9 for the rich, old, and extremely well-studied cluster NGC-2682 (M67). While CG20 stops identifying cluster members at $r_{2D}/\text{pc} \leq 8$, we continue finding members all the way

to $r_{2D}/\text{pc} = 20$, although the rate of increase in source count significantly decreases beyond $r_{2D}/\text{pc} \sim 15$. Interestingly, even within $r_{2D}/\text{pc} = 8$, we identify more members compared to CG20 by a factor of ≈ 2 . Thus, our choice of r_{2D} is not the primary source of the difference in N_{cl} . We find that this difference is also *not* due to the fact that CG20 used DR2 and we, DR3. Even with the DR2 data, our analysis identifies almost the same cumulative source counts as a function of r_{2D} in all clusters. Nevertheless, because of the much-improved uncertainties in DR3, the cluster members we identify naturally exhibit significantly lower fractional errors in $\{\pi, \vec{\mu}\}$ compared to those identified by CG20 (Figure 10). We have tested whether the astrometric parameters, distance, magnitude, and color for the cluster members in our study show any systematic differences compared to these properties for the members identified by CG20 (Figure 11). We find that the D , $\vec{\mu}$ show very similar distributions in both studies, our study simply finds a higher number of members. This implies that the new members we find are not astrometric outliers or coming from the outskirts of the cluster and bolsters our belief that they are genuine members. Nevertheless, a close inspection of the CMDs reveals that CG20 systematically missed a higher fraction of relatively fainter ($G \gtrsim 15$) binary MS sources. MS binaries are of course interesting since they take part in formation of stellar exotica through binary stellar evolution and stellar dynamics (Moe & Stefano 2017; Wang et al. 2020; Mohandasan et al. 2024; El-Badry 2024). It also appears that CG20 missed many sources in the blue straggler region. Blue stragglers are of course very interesting dynamical tracers in a star cluster (Knigge 2015; Ferraro et al. 2023) and if they are there, it is desirable for a member-finding algorithm to identify them. Our member-finding strategy does not depend on the proximity of the sources to any well-defined sequences on the CMD, including the MS. As a result, this strategy may be better suited to identify stragglers.

Similar to the above example, in all of the 21 OCs, the astrometric errors in the members we find are significantly lower because of the shift from DR2 to DR3. Moreover, in all cases, we find that the astrometric properties and D found by this study and CG20 show very similar distributions, peaking roughly at the same values. In 19 of the 21 OCs we have analysed, the comparison of N_{cl} shows exactly the same trends, i.e., we identify more members and *all* members of CG20 are also identified as members by us. The case for Melotte 20 is somewhat different. In this case, the limiting r_{2D} considered by CG20 is 30 pc, significantly higher than ours. As a result, $N_{\text{cl}}/N_{\text{cl},\text{CG20}} < 1$ for Melotte-20.

Table 2 provides a truncated summary for the astrometric and photometric properties of all sources we have analysed within $r_{2D}/\text{pc} \leq 20$ from the 21 clus-

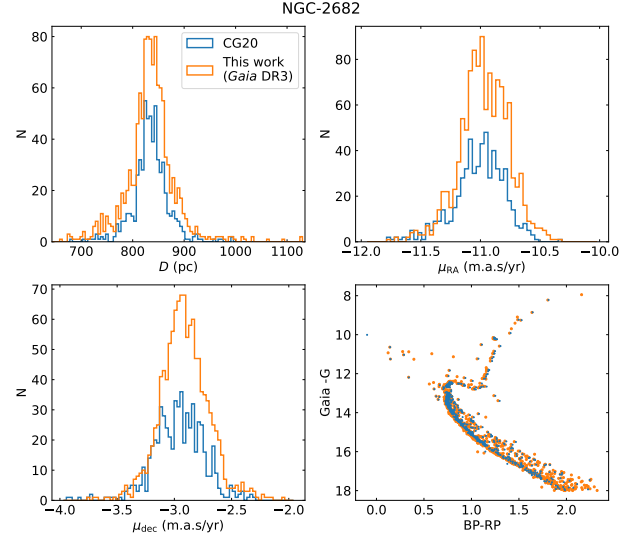


Figure 11. Comparison of the properties of cluster members identified by this study (orange) and CG20 (blue) for NGC 2682. Although we find significantly more members, the members are well-centered in D , μ_{RA} , and μ_{dec} . Comparison of the CMDs denote that we identify several new blue stragglers and many more low-mass stellar binaries compared to those found by CG20 in NGC-2682.

ters. For all sources, independent of whether they are deemed members in our study or not, we provide position, magnitude, color, astrometric properties, our estimated P_{mem} , and the $P_{\text{mem},c}$ we have used for each cluster. Since we provide the estimated P_{mem} for all sources independent of whether we consider them members or not, future studies can easily choose to use a different $P_{\text{mem},c}$ if so desired. The complete machine-readable version is available online.

Most recently, Hunt & Reffert (2023) have used a density-based algorithm HDBSCAN to identify cluster members which they later verify using a CMD classifier based on BNN. They used stars upto $G = 20$ compared to a cut-off of $G = 18$ in our analysis. For an apples-to-apples comparison, we have considered their members up to $G = 18$ and their membership probability $P_{\text{mem,Hunt}} > 0.5$ with those identified by ours.⁶ We find that all our clusters have higher number of members compared to those identified by Hunt & Reffert (2023). The bottom row of Figure 12 shows a comparison of N_{cl} estimated in this study with those given in CG20 and Hunt & Reffert (2023). Interestingly, in the case of NGC-2516, N_{cl} estimated by us match well with the estimate of Hunt & Reffert (2023), both of which

⁶ Note that the membership probabilities obtained from ML algorithms cannot be directly compared with those found by us.

Table 2. List of individual cluster members.

Cluster Name	RA	dec	μ_{RA}	μ_{dec}	π	G	BP-RP	P_{mem}
	(deg)	(deg)	(mas yr ⁻¹)	(mas yr ⁻¹)	(mas)	(mag)	(mag)	
NGC- 2287 $P_{\text{mem}} > P_{\text{mem},c} = 0.96$	102.42	-22.08	-4.48	-1.30	1.37	14.74	1.00	1.00
	102.57	-22.04	-4.69	-0.67	1.88	16.68	1.86	0.99
	101.28	-22.12	-4.57	-1.99	0.96	16.84	1.30	1.00
	⋮	⋮	⋮	⋮	⋮	⋮	⋮	⋮
NGC- 2287 $P_{\text{mem}} < P_{\text{mem},c} = 0.96$	101.10	22.32	-0.35	0.67	0.06	16.40	1.39	0.00
	101.10	22.32	-0.28	5.43	0.60	17.20	1.15	0.00
	101.10	22.32	-1.68	6.95	0.47	15.84	0.79	0.00
	⋮	⋮	⋮	⋮	⋮	⋮	⋮	⋮
NGC- 2682 $P_{\text{mem}} > P_{\text{mem},c} = 0.93$	133.69	11.02	-11.12	-2.91	1.10	14.17	0.82	1.00
	133.46	11.10	-10.93	-2.31	1.20	12.87	0.76	1.00
	133.52	11.35	-10.84	-2.65	1.10	15.45	1.14	1.00
	⋮	⋮	⋮	⋮	⋮	⋮	⋮	⋮
NGC- 2682 $P_{\text{mem}} < P_{\text{mem},c} = 0.93$	133.64	10.81	-33.56	2.57	3.15	12.66	0.89	0.00
	133.64	10.81	-33.11	3.08	3.48	9.28	0.17	0.00
	133.64	10.80	0.73	-8.14	0.88	17.07	1.30	0.00
	⋮	⋮	⋮	⋮	⋮	⋮	⋮	⋮
⋮	⋮	⋮	⋮	⋮	⋮	⋮	⋮	⋮
⋮	⋮	⋮	⋮	⋮	⋮	⋮	⋮	⋮

NOTE— Properties including RA, dec, μ_{RA} , μ_{dec} , π , *Gaia*-G, BP-RP, P_{mem} of all analyzed sources within $r_{\text{proj}}/\text{pc} < 20$ for the 21 OCs we have studied 20 pc region of 21 clusters. For each OC, we also mention the critical P_{mem} , $P_{\text{mem},c}$ above which sources are considered cluster members in this study. The full table can be found in the online version of this manuscript.

are almost three times higher than the estimate given in CG20.

5.2. Cluster properties

Several past studies have provided estimates for the basic cluster properties using various methods. Keeping true to the spirit of this study, we intentionally choose studies that did not focus on specific clusters. Dias et al. (2002) released a catalogue of 1537 OCs and their properties, including coordinates, t_{age} , apparent diameter, colour excess, D , astrometric properties, and $[\text{Fe}/\text{H}]$ based primarily on WEBDA (Lauberts 1982) and ESO (Lynga 1995) catalogues. It is one of the earliest efforts to collect a large number of clusters and their properties inside one single catalogue, which over time became a very useful reference to easily find the properties of a large number of OCs. However, due to the inclusion of data from different surveys, it is difficult to understand the systematics. Indeed, identifying databases obtained from homogeneous analysis of similar quality data can be challenging. For example, while Netopil et al. (2016) estimated $[\text{Fe}/\text{H}]$ for a large number of OCs using spectroscopy, their reported t_{age} was simply estimated by taking the mean of a variety of different past studies. In order to avoid such complications, we carefully investigate past studies and compare our results only with those found by recent studies employing *nearly* homogeneous analysis of similar quality data. Even in recent studies, care is needed to identify the truly independent self-consistent estimates of OC properties. For exam-

ple, Bossini et al. (2019) did not use $[\text{Fe}/\text{H}]$ as a free parameter in their estimations. Instead, they used fixed metallicity values, $[\text{Fe}/\text{H}] = 0$ or values taken directly from Netopil et al. (2016). On the other hand, CG20 results are based on machine learning where the artificial neural network was trained using OC properties reported in Bossini et al. (2019). Most recently, Hunt & Reffert (2023) estimated OC properties using a BNN, where training sets for the CMD classifier were developed based on theoretical isochrones. Hence, we restrict our comparisons mainly to the results of Bossini et al. (2019), CG20, and Hunt & Reffert (2023) for all properties except $[\text{Fe}/\text{H}]$. For $[\text{Fe}/\text{H}]$, we rely on the spectroscopic estimates of Netopil et al. (2016) wherever available. Also, note that the most relevant past estimates come from machine learning. As a result, posteriors or meaningful errorbars are not available for many of the past estimates. As a result, we are forced to resort to by-eye comparisons between our results and the past estimates.

Figure 12 shows a detailed comparison of the cluster properties between our estimates and those in the past studies mentioned above. Where applicable, we show the detailed posterior distributions obtained in our studies (blue violins); the horizontal lines in each violin denote the median, 5th, and 95th percentiles for the posterior distributions. Our estimated t_{age} match well with those estimated in previous studies.

Our estimates for A_v match well with those of Hunt & Reffert (2023) and Bossini et al. (2019), where available.

There are small differences between our estimates with those in CG20 for some OCs. NGC-1647, NGC-2112, and Collinder 261 show the highest levels of mismatch with CG20. In all of these cases, our estimated A_v is higher compared to the estimate of CG20. We notice that these OCs are within $\pm < 16^\circ$ to the galactic plane. Hence, a high level of A_v is not surprising. Interestingly, our estimates match reasonably well with those in [Hunt & Reffert \(2023\)](#) even for these OCs.

Our D estimates show a reasonably good match with all previous studies. Nevertheless, for NGC 6819, NGC 6939, and NGC 7789 our estimates of D are somewhat lower compared to the estimates of CG20 and [Hunt & Reffert \(2023\)](#).

As mentioned earlier, $[\text{Fe}/\text{H}]$ is one of the least addressed topics in past studies. In most cases, it is kept fixed at solar value or previously known values from [Netopil et al. \(2016\)](#). The fourth row from the top of [Figure 12](#), shows the $[\text{Fe}/\text{H}]$ estimates by [Netopil et al. \(2016\)](#). From the smallest to the largest, the green triangles denote photometric, low-resolution (LR), and high-resolution (HR) spectroscopic $[\text{Fe}/\text{H}]$ measurements. Our $[\text{Fe}/\text{H}]$ estimates match well with the estimates of [Netopil et al. \(2016\)](#) for most OCs. Notable exceptions are some old OCs such as Collinder-261, NGC-6939, and NGC-7789, with $\log(t_{\text{age}}/\text{yr}) > 9.5$. For these OCs, our $[\text{Fe}/\text{H}]$ values are lower compared to those given in [Netopil et al. \(2016\)](#). In general, older OCs are expected to have lower $[\text{Fe}/\text{H}]$ (e.g., [Bergemann et al. 2014](#)). Further investigation reveals that the $[\text{Fe}/\text{H}]$ estimates in [Netopil et al. \(2016\)](#) for OCs NGC-6939 (NGC-7789) using HR spectra were based on only 1 (5) star(s), thus, may not be robust. We encourage collection of more HR spectra for more reliable $[\text{Fe}/\text{H}]$ estimates for these old OCs.

6. CONCLUSION

We have developed a non-parametric procedure to identify members of star clusters based on the astrometric parameters found by *Gaia*. In the membership analysis we self-consistently take into account the correlated errors in the astrometric parameters for each source. Once the members are identified, we utilize them to estimate global cluster properties including t_{age} , $[\text{Fe}/\text{H}]$, D , and A_v via isochrone fitting. We have developed a method that eliminates the need for human intervention and subjectivity during isochrone fitting. As a first trial, we have applied these techniques for 21 relatively rich ($N_{\text{cl}} > 500$) and nearby ($D < 3.0$ kpc) clusters identified by CG20 ([section 2](#)). We collect *Gaia* DR3 data from the previously known cluster centers up to $r_{\text{proj}}/\text{pc} = 20$ for the 21 OCs and estimate the membership probabilities P_{mem} for each source. For each OC, we estimate a suitable cut-off membership probability $P_{\text{mem},c}$ based on the P_{mem} distribution of that OC and identify sources with $P_{\text{mem}} > P_{\text{mem},c}$ as cluster members [subsection 3.3](#).

Using these members, we estimate cluster global properties using isochrone fitting in a Bayesian framework without any need for human intervention ([section 4](#)). We identify the single isochrone by first finding the mode of the distribution of sources on the CMD as a function of G and $BP - RP$ ([subsection 4.1](#)). We then find the best-fit polynomial function that goes through the modes and depicts the location of the single-star MS. We use the MIST isochrone ([Dotter 2016; Choi et al. 2016](#)) package to generate theoretical isochrones. We use the *emcee* package ([Foreman-Mackey et al. 2013](#)) to estimate the posterior distributions for the cluster properties t_{age} , $[\text{Fe}/\text{H}]$, D , and A_v by treating them as free parameters with appropriate priors. We summarize our key results below.

- For 19 clusters out of 21, we identify more cluster members than CG20. Our estimated member numbers are higher than those found in [Hunt & Reffert \(2023\)](#) for all 21 OCs we have analyzed. The most likely explanation for this is that these previous studies missed many low-mass MS binaries and straggler sources. The increase in identified cluster members can be as high as a factor of ≈ 2.9 ([subsection 5.1, Table 1](#)).
- We find the full posterior distribution for important cluster properties by simultaneous Bayesian parameter estimation for t_{age} , $[\text{Fe}/\text{H}]$, D , and A_v ([Figure 8](#)). In most cases our estimates agree well with those in relevant previous studies ([subsection 5.2, Figure 12](#)). In some cases we find some differences with likely reasons. For example, for some old OCs our estimated $[\text{Fe}/\text{H}]$ is lower compared to those in [Netopil et al. \(2016\)](#), but in these cases, the estimates in [Netopil et al. \(2016\)](#) were based on very limited number of sources ([subsection 5.2](#)).
- In order to make sure that we do not reject straggler members of an OC, we intentionally do not consider proximity of a source to any well-defined sequence on a CMD. Despite this, our identified members produce excellent clean CMDs. This bolsters our confidence that the members we identify are indeed members of the OCs. Moreover, our method is well-suited to identify straggler members which are important tracers of an OC's dynamical properties.
- Our isochrone fitting procedure does not require any human intervention. Moreover, although we only consider up to the MSTO for isochrone fitting, wherever there is a giant branch, our fitted isochrones simultaneously fits both the MS and the giant branch.

In conclusion, we identify members of 21 rich OCs using a non-parametric data-driven approach which taken

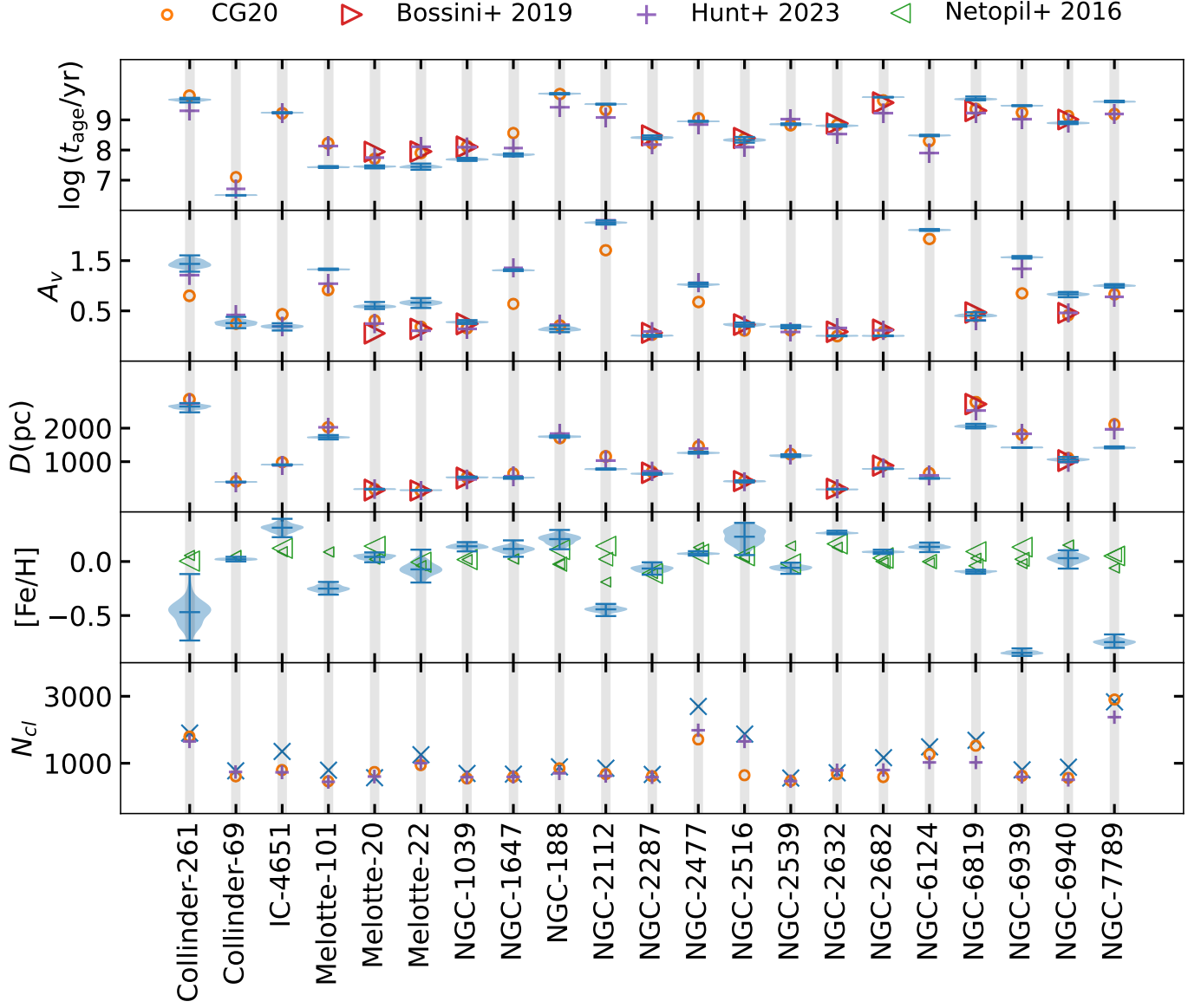


Figure 12. Comparison of cluster properties we estimate with those found in selected past studies (CG20, [Netopil et al. 2016](#); [Bossini et al. 2019](#); [Hunt & Reffert 2023](#)). Cluster names are shown along the horizontal axis. Orange dot, red triangle, violet ‘+’, and green triangle represent values from CG20, [Bossini et al. \(2019\)](#), [Hunt & Reffert \(2023\)](#), and [Netopil et al. \(2016\)](#) respectively. From small to large, the increasing size of the green triangles signifies [Fe/H] estimated using photometry, low-resolution and high-resolution spectroscopy. Blue violins and the horizontal lines denote the posterior distributions, and the median, 5th and 95th percentiles from our Bayesian parameter estimation.

into account correlated errors in astrometric and photometric errors for each source. We identify higher number of members compared to previous studies. Although in this first application of these methods we have restricted ourselves to $r_{\text{proj}}/\text{pc} = 20$, we could easily extend the analysis to much higher r_{proj} . The only limitation is computational cost. Although several OC catalogs exist, often the properties are collected from a variety of studies employing disparate techniques (see discussion in subsection 5.2). In this study we identify OC members and estimate property posterior distributions using methods that requires little subjectivity. Although, we employ our methods to 21 rich and nearby OCs in our first effort, we plan to expand this to more challenging OCs in the future.

AG acknowledges support from TIFR’s graduate fellowship. PKN acknowledges TIFR’s postdoctoral fellowship. PKN also acknowledges support from the Centro de Astrofísica y Tecnologías Afines (CATA) fellowship via grant Agencia Nacional de Investigación y Desarrollo (ANID), BASAL FB210003. SC acknowledges support from the Department of Atomic Energy, Government of India, under project no. 12-R&D-TFR-5.02-0200 and RTI 4002. All simulations are done using Azure cloud computing and TIFR-HPC.

Software : For this work, we extensively use many open software projects like Python 3 (Van Rossum & Drake 2009), Numpy (VanderPlas 2016), scipy (VanderPlas 2016), matplotlib (VanderPlas 2016), pandas (VanderPlas 2016) and Astropy (Astropy Collaboration et al. 2013, 2018)

REFERENCES

- Astropy Collaboration, Robitaille, T. P., Tollerud, E. J., et al. 2013, *A&A*, 558, A33, doi: [10.1051/0004-6361/201322068](https://doi.org/10.1051/0004-6361/201322068)
- Astropy Collaboration, Price-Whelan, A. M., Sipőcz, B. M., et al. 2018, *AJ*, 156, 123, doi: [10.3847/1538-3881/aabc4f](https://doi.org/10.3847/1538-3881/aabc4f)
- Bailer-Jones, C. A. L., Rybizki, J., Foesneau, M., Demleitner, M., & Andrae, R. 2021, *AJ*, 161, 147, doi: [10.3847/1538-3881/abd806](https://doi.org/10.3847/1538-3881/abd806)
- Belokurov, V., Penoyre, Z., Oh, S., et al. 2020, *MNRAS*, 496, 1922, doi: [10.1093/mnras/staa1522](https://doi.org/10.1093/mnras/staa1522)
- Bergemann, M., Ruchti, G. R., Serenelli, A., et al. 2014, *A&A*, 565, A89, doi: [10.1051/0004-6361/201423456](https://doi.org/10.1051/0004-6361/201423456)
- Bhattacharya, S., Vaidya, K., Chen, W. P., & Beccari, G. 2019, *A&A*, 624, A26, doi: [10.1051/0004-6361/201834449](https://doi.org/10.1051/0004-6361/201834449)
- Bossini, D., Vallenari, A., Bragaglia, A., et al. 2019, *A&A*, 623, A108, doi: [10.1051/0004-6361/201834693](https://doi.org/10.1051/0004-6361/201834693)
- Brandner, W., Calissendorff, P., & Kopytova, T. 2023, *MNRAS*, 518, 662, doi: [10.1093/mnras/stac2247](https://doi.org/10.1093/mnras/stac2247)
- Brasser, R., Duncan, M. J., & Levison, H. F. 2006, *Icarus*, 184, 59, doi: [10.1016/j.icarus.2006.04.010](https://doi.org/10.1016/j.icarus.2006.04.010)
- Brogaard, K., Christiansen, S. M., Grundahl, F., et al. 2018, *MNRAS*, 481, 5062, doi: [10.1093/mnras/sty2504](https://doi.org/10.1093/mnras/sty2504)
- Cantat-Gaudin, T. 2022, *Universe*, 8, doi: [10.3390/universe8020111](https://doi.org/10.3390/universe8020111)
- Cantat-Gaudin, T., Vallenari, A., Sordo, R., et al. 2018a, *A&A*, 615, A49, doi: [10.1051/0004-6361/201731251](https://doi.org/10.1051/0004-6361/201731251)
- Cantat-Gaudin, T., Jordi, C., Vallenari, A., et al. 2018b, *A&A*, 618, A93, doi: [10.1051/0004-6361/201833476](https://doi.org/10.1051/0004-6361/201833476)
- Cantat-Gaudin, T., Krone-Martins, A., Sedaghat, N., et al. 2019, *A&A*, 624, A126, doi: [10.1051/0004-6361/201834453](https://doi.org/10.1051/0004-6361/201834453)
- Cantat-Gaudin, T., Anders, F., Castro-Ginard, A., et al. 2020, *A&A*, 640, A1, doi: [10.1051/0004-6361/202038192](https://doi.org/10.1051/0004-6361/202038192)
- Castro-Ginard, A., Jordi, C., Luri, X., et al. 2021, arXiv e-prints, arXiv:2111.01819, <https://arxiv.org/abs/2111.01819>
- Choi, J., Dotter, A., Conroy, C., et al. 2016, *ApJ*, 823, 102, doi: [10.3847/0004-637X/823/2/102](https://doi.org/10.3847/0004-637X/823/2/102)
- Dias, W. S., Alessi, B. S., Moitinho, A., & Lépine, J. R. D. 2002, *A&A*, 389, 871, doi: [10.1051/0004-6361:20020668](https://doi.org/10.1051/0004-6361:20020668)
- Dotter, A. 2016, *ApJS*, 222, 8, doi: [10.3847/0067-0049/222/1/8](https://doi.org/10.3847/0067-0049/222/1/8)
- Dreyer, J. L. E. 1888, *MmRAS*, 49, 1
- El-Badry, K. 2024, *NewAR*, 98, 101694, doi: [10.1016/j.newar.2024.101694](https://doi.org/10.1016/j.newar.2024.101694)
- Ferraro, F. R., Mucciarelli, A., Lanzoni, B., et al. 2023, *Nature Communications*, 14, 2584, doi: [10.1038/s41467-023-38153-w](https://doi.org/10.1038/s41467-023-38153-w)
- Foreman-Mackey, D., Hogg, D. W., Lang, D., & Goodman, J. 2013, *PASP*, 125, 306, doi: [10.1086/670067](https://doi.org/10.1086/670067)
- Gaia Collaboration, Prusti, T., de Bruijne, J. H. J., et al. 2016, *A&A*, 595, A1, doi: [10.1051/0004-6361/201629272](https://doi.org/10.1051/0004-6361/201629272)
- Gaia Collaboration, Vallenari, A., Brown, A. G. A., et al. 2022, arXiv e-prints, arXiv:2208.00211, <https://arxiv.org/abs/2208.00211>
- Geller, A. M., Hurley, J. R., & Mathieu, R. D. 2012, *The Astronomical Journal*, 145, 8, doi: [10.1088/0004-6256/145/1/8](https://doi.org/10.1088/0004-6256/145/1/8)
- Geller, A. M., Leiner, E. M., Chatterjee, S., et al. 2017, *ApJ*, 842, 1, doi: [10.3847/1538-4357/aa72ef](https://doi.org/10.3847/1538-4357/aa72ef)
- Geller, A. M., & Mathieu, R. D. 2011, *Nature*, 478, 356, doi: [10.1038/nature10512](https://doi.org/10.1038/nature10512)
- . 2012, *AJ*, 144, 54, doi: [10.1088/0004-6256/144/2/54](https://doi.org/10.1088/0004-6256/144/2/54)
- Geller, A. M., Leiner, E. M., Bellini, A., et al. 2017, *The Astrophysical Journal*, 840, 66, doi: [10.3847/1538-4357/aa6af3](https://doi.org/10.3847/1538-4357/aa6af3)

- Gosnell, N. M., Mathieu, R. D., Geller, A. M., et al. 2014, *The Astrophysical Journal Letters*, 783, L8, doi: [10.1088/2041-8205/783/1/L8](https://doi.org/10.1088/2041-8205/783/1/L8)
- Grondin, S. M., Drout, M. R., Nordhaus, J., et al. 2024, arXiv e-prints, arXiv:2407.04775, doi: [10.48550/arXiv.2407.04775](https://doi.org/10.48550/arXiv.2407.04775)
- Hunt, E. L., & Reffert, S. 2021, *A&A*, 646, A104, doi: [10.1051/0004-6361/202039341](https://doi.org/10.1051/0004-6361/202039341)
- . 2023, *A&A*, 673, A114, doi: [10.1051/0004-6361/202346285](https://doi.org/10.1051/0004-6361/202346285)
- Jadhav, V. V., Roy, K., Joshi, N., & Subramaniam, A. 2021, *AJ*, 162, 264, doi: [10.3847/1538-3881/ac2571](https://doi.org/10.3847/1538-3881/ac2571)
- Jeffery, E. J., von Hippel, T., van Dyk, D. A., et al. 2016, *ApJ*, 828, 79, doi: [10.3847/0004-637X/828/2/79](https://doi.org/10.3847/0004-637X/828/2/79)
- Johnson, H. L., & Sandage, A. R. 1955, *ApJ*, 121, 616, doi: [10.1086/146027](https://doi.org/10.1086/146027)
- Jorissen, A. 2019, *Mem. Soc. Astron. Italiana*, 90, 395
- Knigge, C. 2015, in *Astrophysics and Space Science Library*, Vol. 413, *Astrophysics and Space Science Library*, ed. H. M. J. Boffin, G. Carraro, & G. Beccari, 295, doi: [10.1007/978-3-662-44434-4_13](https://doi.org/10.1007/978-3-662-44434-4_13)
- Knigge, C., Leigh, N., & Sills, A. 2009, *Nature*, 457, 288, doi: [10.1038/nature07635](https://doi.org/10.1038/nature07635)
- Kounkel, M., Covey, K., & Stassun, K. G. 2020, *AJ*, 160, 279, doi: [10.3847/1538-3881/abc0e6](https://doi.org/10.3847/1538-3881/abc0e6)
- Kruijssen, J. M. D., Pelupessy, F. I., Lamers, H. J. G. L. M., Portegies Zwart, S. F., & Icke, V. 2011, *MNRAS*, 414, 1339, doi: [10.1111/j.1365-2966.2011.18467.x](https://doi.org/10.1111/j.1365-2966.2011.18467.x)
- Lada, C. J., & Lada, E. A. 1991, in *Astronomical Society of the Pacific Conference Series*, Vol. 13, *The Formation and Evolution of Star Clusters*, ed. K. Janes, 3–22
- Lauberts, A. 1982, *ESO/Uppsala survey of the ESO(B) atlas*
- Leigh, N. W. C., Panurach, T., Simunovic, M., et al. 2019, *MNRAS*, 482, 231, doi: [10.1093/mnras/sty2707](https://doi.org/10.1093/mnras/sty2707)
- Leiner, E., Mathieu, R. D., & Geller, A. M. 2017, *ApJ*, 840, 67, doi: [10.3847/1538-4357/aa6aff](https://doi.org/10.3847/1538-4357/aa6aff)
- Leiner, E. M., & Geller, A. 2021, *The Astrophysical Journal*, 908, 229, doi: [10.3847/1538-4357/abd7e9](https://doi.org/10.3847/1538-4357/abd7e9)
- Lindgren, L., Hernández, J., Bombrun, A., et al. 2018, *A&A*, 616, A2, doi: [10.1051/0004-6361/201832727](https://doi.org/10.1051/0004-6361/201832727)
- Lynga, G. 1995, *VizieR Online Data Catalog*, VII/92A
- Moe, M., & Stefano, R. D. 2017, *The Astrophysical Journal Supplement Series*, 230, 15, doi: [10.3847/1538-4365/aa6fb6](https://doi.org/10.3847/1538-4365/aa6fb6)
- Mohandasan, A., Milone, A. P., Cordoni, G., et al. 2024, *A&A*, 681, A42, doi: [10.1051/0004-6361/202347424](https://doi.org/10.1051/0004-6361/202347424)
- Monteiro, H., & Dias, W. S. 2019, *Monthly Notices of the Royal Astronomical Society*, 487, 2385, doi: [10.1093/mnras/stz1455](https://doi.org/10.1093/mnras/stz1455)
- Monteiro, H., Dias, W. S., Hickel, G. R., & Caetano, T. C. 2017, *NewA*, 51, 15, doi: [10.1016/j.newast.2016.08.001](https://doi.org/10.1016/j.newast.2016.08.001)
- Netopil, M., Paunzen, E., Heiter, U., & Soubiran, C. 2016, *A&A*, 585, A150, doi: [10.1051/0004-6361/201526370](https://doi.org/10.1051/0004-6361/201526370)
- Nine, A. C., Milliman, K. E., Mathieu, R. D., et al. 2020, *The Astronomical Journal*, 160, 169, doi: [10.3847/1538-3881/abad3b](https://doi.org/10.3847/1538-3881/abad3b)
- Pal, H., & Jadhav, V. 2024, in 42nd meeting of the Astronomical Society of India (ASI, P187
- Parmentier, G., & Pfalzner, S. 2013, *A&A*, 549, A132, doi: [10.1051/0004-6361/201219648](https://doi.org/10.1051/0004-6361/201219648)
- Pfalzner, S., Kaczmarek, T., & Olczak, C. 2012, *A&A*, 545, A122, doi: [10.1051/0004-6361/201219881](https://doi.org/10.1051/0004-6361/201219881)
- Rain, M. J., Carraro, G., Ahumada, J. A., et al. 2020, *The Astronomical Journal*, 161, 37, doi: [10.3847/1538-3881/abc1ee](https://doi.org/10.3847/1538-3881/abc1ee)
- Sahu, S., Subramaniam, A., Simunovic, M., et al. 2019, *ApJ*, 876, 34, doi: [10.3847/1538-4357/ab11d0](https://doi.org/10.3847/1538-4357/ab11d0)
- Sandage, A. R. 1953, *AJ*, 58, 61, doi: [10.1086/106822](https://doi.org/10.1086/106822)
- Sarajedini, A., von Hippel, T., Kozhurina-Platais, V., & Demarque, P. 1999, *AJ*, 118, 2894, doi: [10.1086/301149](https://doi.org/10.1086/301149)
- Scott, D. W. 2015, *Multivariate Density Estimation: Theory, Practice, and Visualization*, 2nd Edition, Wiley Series in Probability and Statistics (WILEY)
- Sindhu, N., Subramaniam, A., Jadhav, V. V., et al. 2019, *ApJ*, 882, 43, doi: [10.3847/1538-4357/ab31a8](https://doi.org/10.3847/1538-4357/ab31a8)
- Thompson, B., Frinchaboy, P., Kinemuchi, K., Sarajedini, A., & Cohen, R. 2014, *AJ*, 148, 85, doi: [10.1088/0004-6256/148/5/85](https://doi.org/10.1088/0004-6256/148/5/85)
- Tofflemire, B. M., Gosnell, N. M., Mathieu, R. D., & Platais, I. 2014, *AJ*, 148, 61, doi: [10.1088/0004-6256/148/4/61](https://doi.org/10.1088/0004-6256/148/4/61)
- Vaidya, K., Rao, K. K., Agarwal, M., & Bhattacharya, S. 2020, *Monthly Notices of the Royal Astronomical Society*, 496, 2402, doi: [10.1093/mnras/staa1667](https://doi.org/10.1093/mnras/staa1667)
- Van Rossum, G., & Drake, F. L. 2009, *Python 3 Reference Manual* (Scotts Valley, CA: CreateSpace)
- VanderPlas, J. 2016, *Python Data Science Handbook: Essential Tools for Working with Data*, 1st edn. (O'Reilly Media, Inc.)
- Virtanen, P., Gommers, R., Oliphant, T. E., et al. 2020, *Nature Methods*, 17, 261, doi: [10.1038/s41592-019-0686-2](https://doi.org/10.1038/s41592-019-0686-2)
- von Hippel, T., Jefferys, W. H., Scott, J., et al. 2006, *ApJ*, 645, 1436, doi: [10.1086/504369](https://doi.org/10.1086/504369)
- von Hippel, T., & Sarajedini, A. 1998, *AJ*, 116, 1789, doi: [10.1086/300561](https://doi.org/10.1086/300561)

Wang, C., Langer, N., Schootemeijer, A., et al. 2020, The
Astrophysical Journal Letters, 888, L12,
doi: [10.3847/2041-8213/ab6171](https://doi.org/10.3847/2041-8213/ab6171)

APPENDIX

A. SURFACE DENSITY PROFILE

We estimated the surface density profile of cluster members and all stars (field and cluster) in the vicinity of the cluster. In Figure 13, all the red dots show the cluster surface density profile and all the blue dots show all stars' surface density profile. The black horizontal solid line shows the average density of all stars in the 15-20 pc region of NGC-2287. The grey-shaded region is the corresponding error bar. From this, we notice the cluster surface density profile falls to a much lower value compared to the all-star density before reaching the 20 pc radial value.

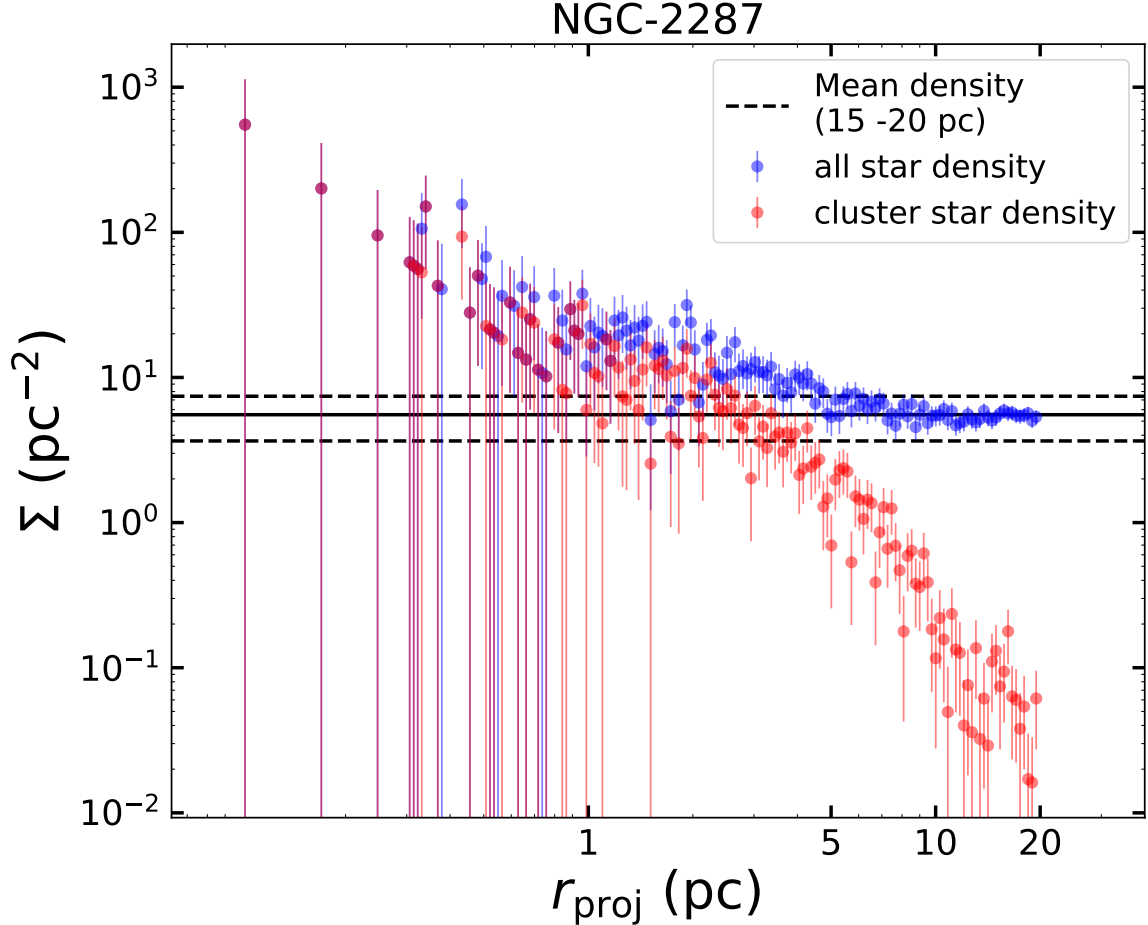


Figure 13. Surface density (Σ) profile for NGC 2287. Blue and red dots denote the surface density profiles for all sources and cluster members, respectively. The black solid line and the grey-shaded region show the mean Σ for all sources within $15 \leq r_{\text{proj}}/\text{pc} \leq 20$ and the corresponding 1σ errors. We find that the Σ for cluster members becomes smaller than that for all sources at r_{proj} significantly smaller than 20 pc. This behavior is found in all 21 OCs we have analyzed.

B. CONVERGENCE TEST

In our Bayesian analysis, we perform MCMC samplings for 60000 steps with 128 walkers. We discard the first 30000 walker as a burn-in step. Then we create two batches of walkers- one from 40000 to 50000 step and the other is 50000 to 60000 steps. In Figure 14, we plot both the walker distributions and notice that the distributions are identical. This signifies that our walkers have converged to the final values of the cluster parameters.

NGC-2287

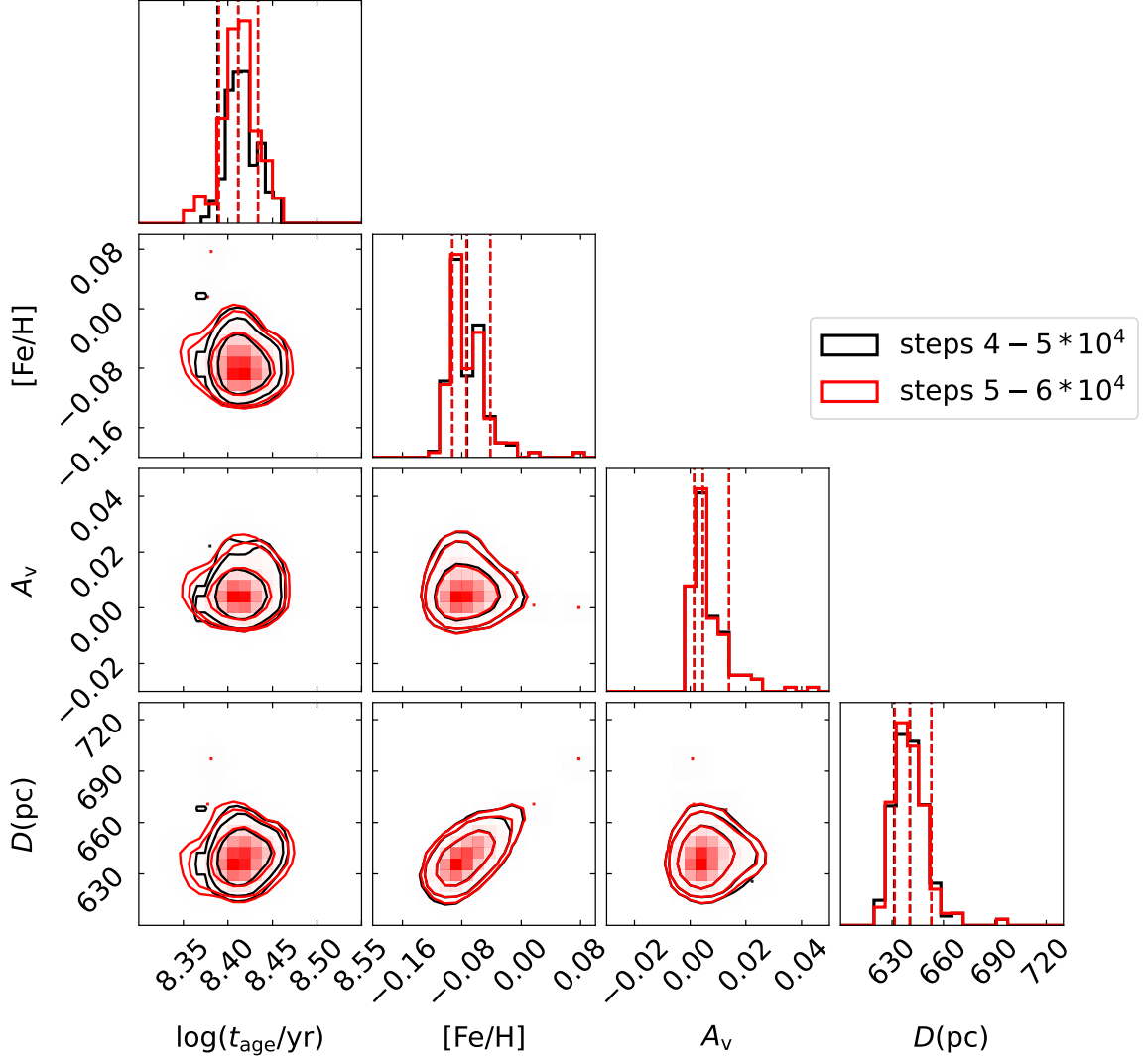


Figure 14. Same as Figure 8 but showing convergence in our Bayesian parameter estimation for NGC-2287. We show one and two-dimensional marginalized posterior distributions for steps 40000–50000 (black) and 50000–60000 (red). Both distributions show excellent agreement. Hence, we infer that our MCMC chains have sufficiently converged.

C. DEPENDENCY ON MEMBERSHIP

We investigate how the cluster global properties may change with different cluster membership cutoff values. We collect the cluster members for different cluster membership values and use them in our Bayesian framework to estimate cluster properties. We show in Figure 15 that the final posterior distribution of cluster properties is almost the same for different membership cutoff values.

NGC -2287

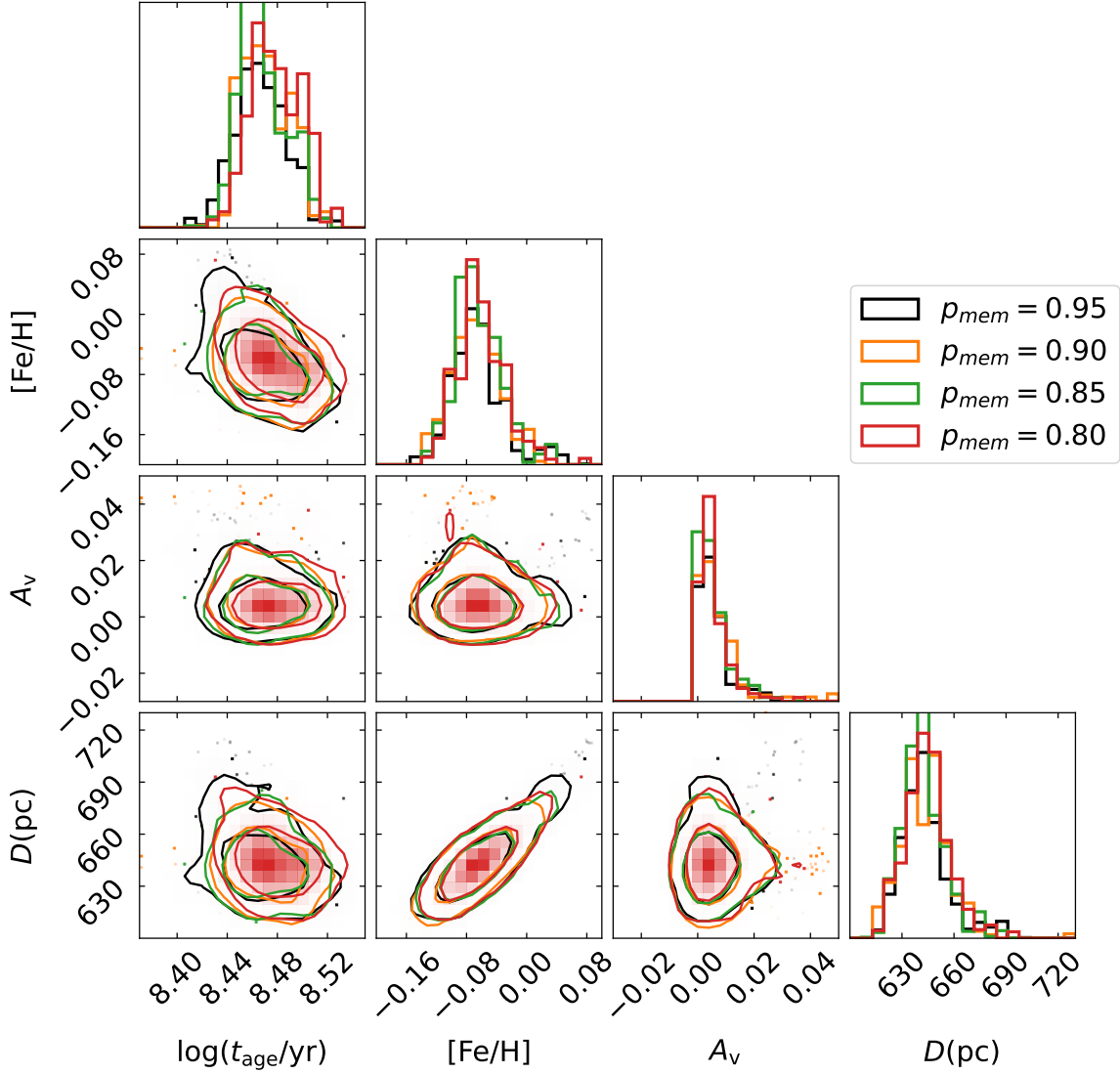


Figure 15. Same as Figure 8 but showing the effect of adopted $P_{\text{mem},c}$ on the estimated cluster properties t_{age} , $[\text{Fe}/\text{H}]$, A_v , and D . The different colors denote different adopted $P_{\text{mem},c}$ (see legend). We find that the adopted $P_{\text{mem},c}$ (within reason) does not affect the final posterior distributions of cluster properties.